

### 3. PARTICIPATION IN THE USE OF THE JET FACILITIES BY THE EFDA ASSOCIATES

F. Serra (Head), D. Borba, M.E. Manso, M.F. Nave, V. Plyusnin, F. Salzedas, C. Silva, L. Fattorini, D. Alves, P. Belo, R. Coelho, S. Cortes, N. Cruz, A. Figueiredo, B. Gonçalves, L. Meneses, I. Nedzelski, F. Nabais, T. Ribeiro, J. Sousa, P. Varela, I. Nunes

#### 3.1. INTRODUCTION

The Association EURATOM/IST has proceeded with its participation in the collective use of the JET Facilities, in the frame of the “European Fusion Development Agreement” (EFDA) through the “JET Operation Contract” and the “JET Implementing Agreement”.

This chapter presents the main activities carried out during this year in the areas of:

- Operation;
- Scientific exploitation;
- Enhanced Performance Project;
- Management.

#### 3.2. OPERATION

Three members of the IST/CFN staff have been involved in the JET operation:

- Dr. Sebastien Hacquin has participated in the JET Operation Team, through a Secondment Agreement with the Association EURATOM/UKAEA, working in the Reflectometry and LIDAR Diagnostics Group. The main activities carried out under the JOC position were<sup>1</sup>:
  - Operation and maintenance of both the X-mode correlation reflectometer ( kg8b) and the O-mode reflectometer (KG3);
  - Data validation and analysis of the KG8b and KG3 (O-mode reflectometer) diagnostics;
  - Reprocessing of KK3 radiometer ECE data from a calibration with KK1 Michelson Interferometer data in order to extract the electronic temperature profile.
- Mr. Luis Meneses and Mr. Nuno Cruz have provided technical support to the operation and maintenance of the correlation reflectometer.

#### 3.3. SCIENTIFIC EXPLOITATION

##### 3.3.1. Introduction

The participation in the JET 2003 Work Programme had contributions from fifteen scientists to the experimental campaigns C8-C12 at the JET site (Table 3.1). The work was focused on code developments and physics studies related mainly with Task Forces M, D and E.

<sup>1</sup> Besides the above activities Dr. S. Hacquin has also participated in the experimental campaigns for the scientific exploitation of the diagnostics (Table 3.1 and section 3.3.3).

#### 3.3.2. Work within Task Force M, plus support to S1,S2 and T

##### 3.3.2.1 Use of ICRH in JET discharges for the prevention of core impurity accumulation.

The use of ICRH has been extended to high triangularities ( $\delta > 0.4-0.5$ ), high density, ELMy H-mode plasmas both with and without impurity injection. The ICRH is now used routinely in impurity injection radiative mantle experiments in ITER-like configurations to increase discharge stationarity. Also, impurity accumulation associated with sawtooth loss has been controlled with ICRH, in recent JET experiments exploring a type I-type II ELM regime in ITER-like and Quasi-Double-Null configurations.

Research continued on the understanding of how using ICRH benefits plasma performance. Increasing power in the plasma core maintains sawtooth MHD activity and their beneficial effect in re-distributing impurities. However, other mechanisms affecting impurity transport may also contribute to impurity control. A higher temperature would increase Ar ionization, leading to a decreased radiation from the central region. In addition, the improved power balance may alter impurity transport. Experimental results were compared with predictions from the neoclassical impurity accumulation model of Tokar et al (1977). In the JET experiments considered, Argon was found to be in the Pfirsch-Schluter collisionality regime. In the model, a critical heating power density,  $Q_{crit}$ , is introduced, below which a development of the impurity instability is expected:

$$Q_{heat} \leq Q_{crit} = C \frac{D_{neo}}{D_{\perp}} Z_I Q_{rad} \quad (3.1)$$

where  $Q_{heat}$  and  $Q_{rad}$  are the central heating power and central radiation power densities.  $C$  is of order 1 (depending on profile effects),  $Z_I$  is the charge of the impurity (in our case of Argon not fully ionized:  $Z_I \approx 16$ ). In order to test this criterion, the power balance in the plasma core was studied (Figure 3.1) for high Ar rate discharges with and without ICRH. The heating power density was calculated using TRANSP, while the radiative heating density was obtained from bolometry measurements.

Name	Competence	1 <sup>st</sup> Stay		2 <sup>nd</sup> Stay		3 <sup>rd</sup> Stay	
		Start	End	Start	End	Start	End
Duarte Borba	TFL, MHDAE	31 March	2 May	18 Aug	16 Sept	-	-
M. Filomena Nave	TSL, SL, MHDAE	24 Feb	23 May	18 Aug	31 Oct	24 Nov	19 Dec
Paula Belo	IEMHDA, CATS	10 March	16 April	18 Aug	31 Oct	24 Nov	19 Dec
Fernando Nabais	FPE	17 March	16 May	18 Aug	31 Oct	24 Nov	19 Dec
Vladislav Plyusnin	MHDME	4 March	17 April	1 Sept	16 Sept	-	-
Carlos Silva	KY3	3 March	21 March	28 April	16 May	-	-
Rui Coelho	SEFDT, NTME	31 March	17 April	1 Sept	16 Sept	-	-
Jorge Ferreira	PTM	18 Aug	5 Sept	4 Nov	9 Dec	-	-
Santiago Cortes	KS9	31 March	4 April	12 Aug	5 Sept	-	-
Luca Fattorini	KG8b	7 April	17 April	13 Oct	31 Oct	-	-
Ricardo Galvão	MHDAE	13 Oct	31 Oct	24 Nov	5 Dec	-	-
Isabel Nunes	KG8b	24 Nov	19 Dec	-	-	-	-
Igor Nedzelski	KY3	31 March	16 April	-	-	-	-
Diogo Alves	KS9	24 Feb	16 May	22 Sep	31 Oct	24 Nov	19 Dec
Sebastien Hacquin	JOC+S/T Tasks (88 Days)						

Table 3.1 – Portuguese participation in the 2003 JET campaigns

The critical power density  $Q_{crit}$  was estimated taking sawtooth-averaged diffusion coefficients  $\frac{D_{neo}}{D_{\perp}} \approx 0.2$ .

In the reference discharge (NBI only),  $Q_{rad}$  started to increase slowly at  $t \sim 0.75$  s. When the sawteeth disappeared,  $t > 1.3$  s,  $Q_{crit}$  exceeded  $Q_{heat}$ . Thus the sudden impurity accumulation that followed could be explained, within experimental data uncertainties, on the basis of the instability proposed in the model. Also an increase of the heat power density would prevent impurity accumulation. When the heating power density was increased by ICRH,  $Q_{crit}$  was always below the actual heating power density  $Q_{heat}$  (Figure 3.1). From this study it has been concluded that a combination of MHD and temperature screening effects may have prevented impurity accumulation in discharges with added ICRH.

### 3.3.2.2. Sawtooth experiments with counter NBI

During the operation with reverse toroidal field, experiments to study the sawtooth instability with NBI heating were performed. In JET, reversing the  $B_T$  direction changes the NBI heating to counter injection, while the usual field operation has co-NBI. The object of the experiments was twofold: a) to explore ways of reducing sawtooth period in JET and ITER plasmas; b) to study rotation effects on sawtooth stability. Plasmas with matched  $B_T$ ,  $I_p$  and shape (high wall clearance was needed for reversed  $B_T$  operation.) were produced in the reversed and the usual  $B_T$  machine configurations. NBI power was varied up to 13 MW. The experiment included a power scan at constant density. In addition the effects of normal and tangential injection were investigated. These experiments confirmed earlier JET results that short ST periods, smaller than in the Ohmic regime, can be obtained with counter-NBI injection (Figure 3.2). This has positive implications

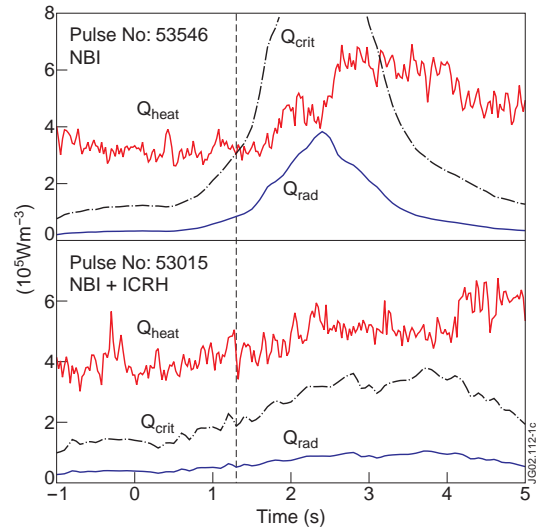


Figure 3.1 – Volume averaged power densities at  $\Psi = 0.1$  plotted against time, where  $t = 0$  is the start of the after-puff phase.  $Q_{heat}$  is the heating power calculated by TRANSP,  $Q_{rad}$  is the radiated power measured by the bolometers. The critical power density,  $Q_{crit}$  was estimated taking sawtooth averaged diffusion coefficients  $\frac{D_{neo}}{D_{\perp}} \approx 0.2$ . Sawteeth in the discharge with NBI only stopped at  $t = 1.3$  s (indicated by dotted line).

for achieving good plasma confinement. Reducing the sawtooth period in JET H-mode experiments is known to provide better control of NTMs. It can also provide better control of core impurity accumulation in high-density ELMy H-mode plasmas. The smallest sawteeth periods were observed with reversed  $B_T$  and normal NBI. The study of the sawtooth behaviour as a function of power has yielded a new result. Unlike, co-NBI where the observed ST period increases with power, with counter-NBI a minimum has been found at 4 MW (Figure 3.2). A similar

trend is observed with toroidal plasma rotation. With co-NBI the sawtooth period increased with core plasma rotation. With counter-NBI the sawtooth period reduced to a minimum for central plasma rotation at  $\sim 2$  kHz. With reversed  $B_T$ , the toroidal  $\vec{E} \times \vec{B}$  rotation is in opposition to characteristic frequencies  $\omega_{*i}$  and  $\langle \omega_{*i} \rangle$ .

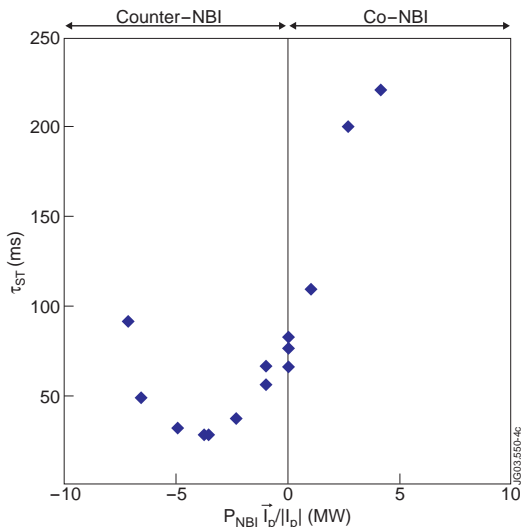


Figure 3.2 - Sawtooth period vs  $P_{NBI}$  from a power scan at constant density using mainly normal NBI ( $B_T=2.7$  T,  $I_p=2.5$  MA,  $q_{95}=3.6$ ). With co-NBI the sawtooth period increased with power. With counter-NBI the sawtooth period reduced to a minimum at 4 MW.

Plasma rotation in the core of the plasma is reduced when compared with co-NBI. A candidate mechanism consistent with the main features of the observations is the dependence of the internal kink stability on sheared toroidal rotation.

Kinetic effects from sheared counter rotation in a regime where the mode frequency  $\omega \sim \omega_{*i} \sim \omega_{di}$ , are expected to be destabilizing. Reversed q shear with  $q_{min} < 1$  from NBI current drive was suggested as an explanation for previous JET observations. For recent experiments, this can be ruled out, since q-profile analysis from MSE measurements indicated that q-profiles are peaked.

### 3.3.2.3 Statistical study of neo-classical tearing modes onset

The first statistical work for the NTM onset (in JET 1999 experiments) found a clear correlation between the onset and the sawtooth crash, and a linear correlation between  $\beta_N$  and normalized ion Larmor radius,  $\rho_{i*} = \rho_i/a$ . Between 2000 and 2001, JET experiments on controlling the NTM by controlling the sawtooth period found a correlation between the onset for  $\beta_N$  NTMs and the sawtooth period. The NTM is destabilized at a higher  $\beta_N > 2$  for shorter

periods and vice-versa. This does not explain the cases where the onset is clear before the crash and during the sawtooth precursor. This suggests that the seed island formation could be from a non-linear mode coupling with the  $n=1$  or toroidal coupling with  $n=2$  component of the sawtooth precursor.

A statistical analysis on the (3,2) NTM onset was performed using a database of pulses between 1999 and 2002 (total of 153 pulses). The database includes ELM modes regimes for ICRH dominantly heated plasmas, NBI and the combination of both. This statistical work was compared with a database with 123 pulses in ELM mode regime where the (3,2) NTM was not observed.

The statistical work consists of the study on the relation between  $\beta_N$  and  $\rho_{i*}$ ; the (1,1) mode amplitude of the fishbone instabilities or sawtooth precursors nearest to the NTM onset and the plasma parameters relevant to the NTM model; the sawtooth period and  $\beta_N$ .

Using the (1,1) mode frequency at the onset fishbone for mode triples, the trend line (Figure 3.3) is closer to the ideal match than the one from sawtooth (via three-wave non-linear coupling with the (1,1) sawtooth precursor and the (4,3) NTM, which is always present at the driven mode (3,2) onset). This indicates a stronger possibility for the three-mode coupling to be with the fishbone oscillations rather than the sawtooth. This shows the importance of the fishbone instability for the seed island driven mode, and it is necessary to take into account when trying to control the NTMs by sawtooth control.

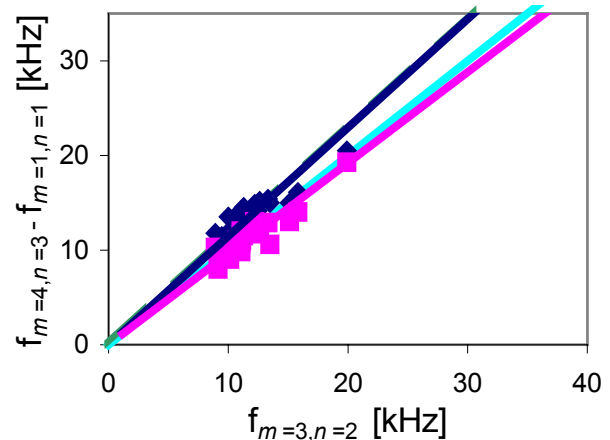


Figure 3.3 - Frequency of the (3,2) NTM versus the difference between the frequency of the (3,2) mode and the maximum (pink) and minimum (blue) frequencies of the fishbone instabilities. The trend line is related to the sawtooth (green) and the line of perfect frequency matching (light blue).

### 3.3.2.4 Impurity penetration through the edge transport barrier

JET has performed experiments in which controlled influx of noble gas impurities was successfully used in order to reduce the amplitude and frequency of type-I ELMs. An

interesting correlation between the level of the main gas puffing and the radial redistribution of impurities has been found. It was shown that reduction of the puffing below a certain level leads to impurity accumulation in the core followed by thermal collapse. Figure 3.4 shows the main time traces for discharge #53550 with Ar seeding and a monotonically decreasing level of the main gas puffing. One can observe that the radiated power starts to grow rapidly once the main gas puffing rate drops below some critical level. The application of Ar seeding (which starts at  $t = 20$  s) leads to an increase in the level of radiated power (b), which is immediately followed by the reduction in ELM frequency. Note that for the first 2-3 seconds of Ar seeding there is no detrimental effect of the radiation on the energy content (a).

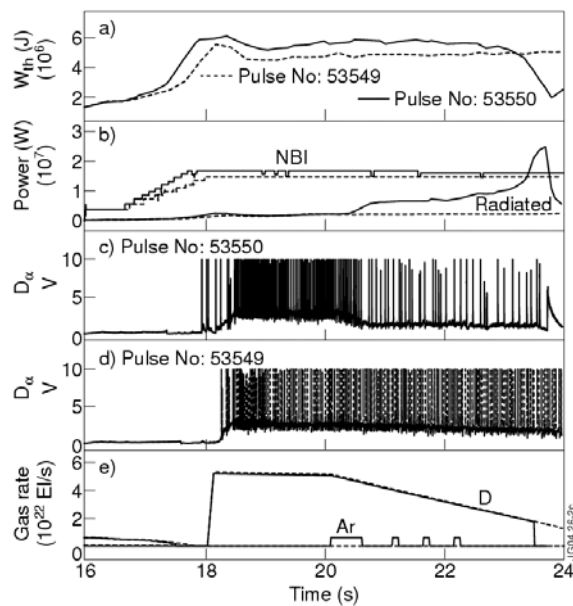


Figure 3.4 - Plasma parameters for the Ar seeded shot #53550 (full line) and reference shot #53549 without Ar (dashed line)

In the theoretical modeling both anomalous and neoclassical transport models were considered to contribute to the impurity transport. For the anomalous transport an empirical Bohm/gyroBohm model [Cherubini et al., 1996] was used. Neoclassical transport plays an important role mainly in two plasma regions: at the core and at the edge transport barrier where the anomalous transport is reduced. JETTO (1.5 D core transport for main ions) and SANCO (1D transport code for impurities) were used. JETTO+SANCO checks the normalised pressure gradient

$$\alpha \equiv \frac{-2\mu_0 R q^2}{B_\phi^2} \cdot \frac{\partial p}{\partial r} \quad (3.2)$$

within the ETB and compares it with the critical parameter  $\alpha_{crit}$ , which destabilises the ballooning mode. The sawtooth reconnection was also considered in the modelling. To

simulate the experimentally observed disappearance of sawteeth in a later phase of the shot #53550 (with impurity injection) the sawtooth reconnection model is turned off at  $t = 23$  s (in both runs with impurity injection). Figure 3.5 shows the main time traces for two simulations. The same level of Ar puffing was used in both runs. Starting from  $t = 21.5$  s, the edge density goes down and the edge temperature goes up in “red” case. This gradual change in the boundary conditions causes a dramatic transformation in impurity behaviour: they start to penetrate through the edge transport barrier and accumulate in the core. The reason for such transformation is the convective velocity for impurities, which changes sign from positive to negative within the edge barrier. Figure 3.6 shows the radial distribution of the convective velocity,

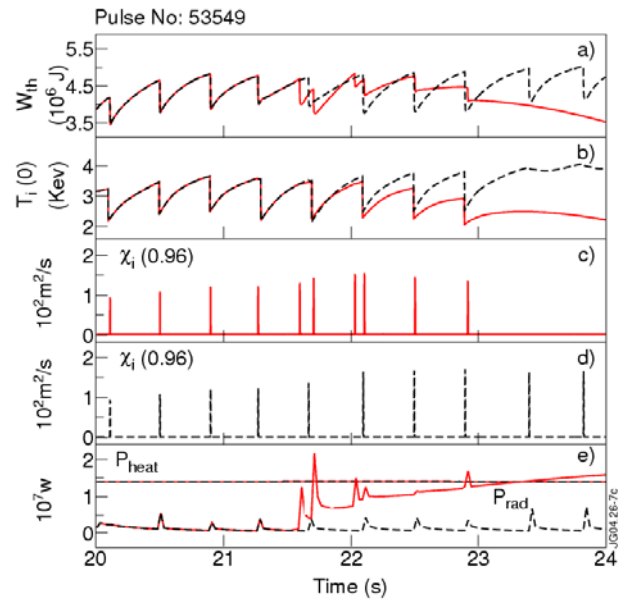


Figure 3.5 - Time traces for the run with the same rate of impurity puff but different boundary conditions: constant temperatures and density (black) and rising temperature and falling density (red).

averaged over all ionisation stages, and the impurity density for two time slices:  $t = 21$  s and  $t = 23$  s for shot #53550. At 21.0 s the two runs have the same boundary conditions and both have the same positive convective velocity, leading to an accumulation of impurities outside separatrix, in the SOL. At  $t = 23$  s after the step down in the edge density and step up in the edge temperature in the “red” case, the convective velocity for #53550 has a different, negative sign. This allows impurities to penetrate through the ETB and to accumulate deeper in the core, changing both the level and the pattern of the radiated power. From the simulations higher level of core radiation effectively reduces the heat flux across the separatrix and results in a decrease of ELMs frequency until its complete disappearance on the later stage of the discharge.

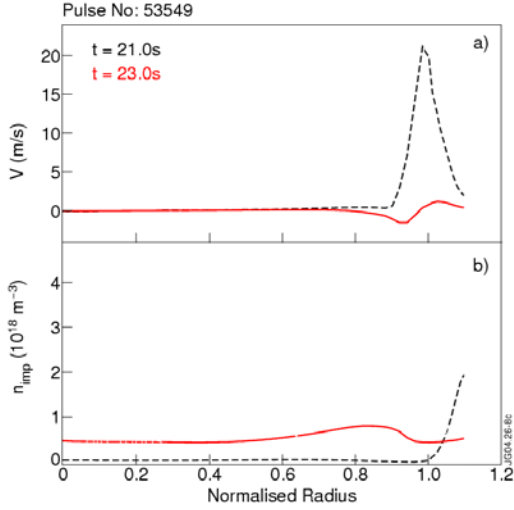


Figure 3.6 - Radial distribution of convective velocity density of impurity before (black) and after (red) transition to a lower level of gas puffing.

For these two runs the ELMs make different contributions to the impurity transport. Each ELM drives the impurity toward the centre in the “black” case of strong gas puffing (Figure 3.7). However, the impurity content both in the SOL and in the core recovers its pre-ELM level in 50 ms after the end of ELM. Keeping in mind that experimentally observed ELM repetition rate is very low,  $\Delta t_{\text{ELM}}=210$  ms, we conclude that transport between ELMs is more important for impurity redistribution than transport during the ELM in type-I ELMy H-mode JET plasmas. It is worth noting here that ELMs are usually considered as beneficial factor, which keeps impurities away from the core. The modelling shows, however, that if ELMs have a diffusive nature, they can actually drive impurities toward the plasma core as well.

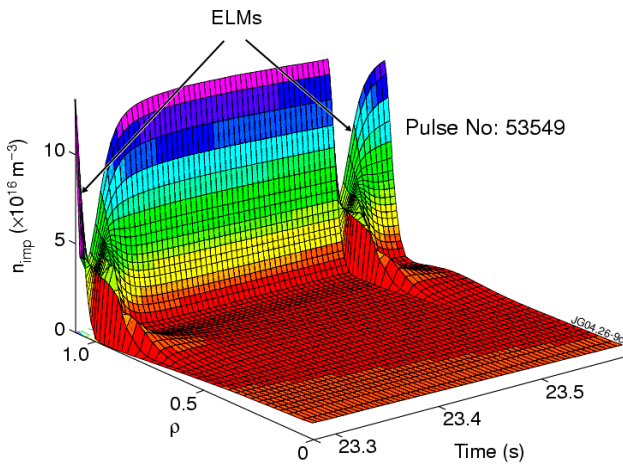


Figure 3.7 - Evolution in time of the impurity density profiles between two ELMs for the “black” case.

### 3.3.2.5 Sawtooth stabilization by ICRH driven fast ions as function of global parameters

One of the most promising methods for sawtooth control is based on the use of Ion Cyclotron Resonance Heating (ICRH). Stabilization of sawteeth depends on the fast ions distribution function as well as on the mode eigenfunction and equilibrium conditions. However, for practical purposes it is convenient to determine conditions for stabilization as function of global parameters.

Experimentally, K. McClements *et al*, found the existence of thresholds for sawtooth stabilization as function of both the ICRH injected power  $P_{\text{ICRH}}$ , and the plasma density  $n_e$ . According to the Stix model both  $P_{\text{ICRH}}$  and  $n_e$  directly influence the fast ions temperature, 
$$T_{\text{HOT}} \propto \frac{\langle P_{\text{ICRH}} \rangle T_e^{3/2}}{3n_e n_{\text{HOT}}}.$$

It is known that fast ion populations can only exert an effective stabilizing influence on the internal kink mode if the fast ion temperature  $T_{\text{HOT}}$  is much higher than that of the bulk ions  $T_i$ . This establishes a lower threshold in  $T_{\text{HOT}}$  below which stabilization does not occur. On the other hand, since the stabilizing influence of ICRH driven fast ions over sawteeth is known to weaken at high fast ions temperatures, an upper threshold in  $T_{\text{HOT}}$  above which stabilization does not occur must also exist. This explains why stabilization is not observed for values of  $P_{\text{ICRH}}$  exceedingly high or for values of  $n_e$  exceedingly low. The thresholds in  $P_{\text{ICRH}}$  and  $n_e$  are correlated and can be replaced by a single threshold in  $P_{\text{ICRH}}/n_e$ . For on-axis heating,  $\Lambda \equiv \mu B_0/E \approx 1$ , it is then possible to establish regions of stabilization as function of the global parameters  $P_{\text{ICRH}}$  and  $n_e$  (Figure 3.8). The upper thresholds were plotted using experimental data from the JET tokamak. A lower threshold below which the fast ions temperature is too low to provide efficient stabilization of the internal kink was roughly estimated using the Stix formula and the numerical results calculated with the CASTOR-K code.

From the results in Figure 3.8 it is possible to explain sawtooth behaviour in JET low density discharges (#47576 and #54300 to #54306) where sawtooth stabilization is initially observed, being lost during the discharge and reoccurring later. Figure 3.9 shows typical sawtooth behaviour, for the case of #47576 (#47575 being the reference discharge). Sawteeth are stable in the initial phase of the heating ramp. When  $P_{\text{ICRH}}$  exceeds a threshold value, sawteeth become unstable. Later in the discharge the plasma density increases, so the threshold in  $P_{\text{ICRH}}$  required in order to keep sawteeth unstable also increases. At some point the threshold is crossed again in the opposite direction due to the increase in the plasma density and sawteeth are stabilized.

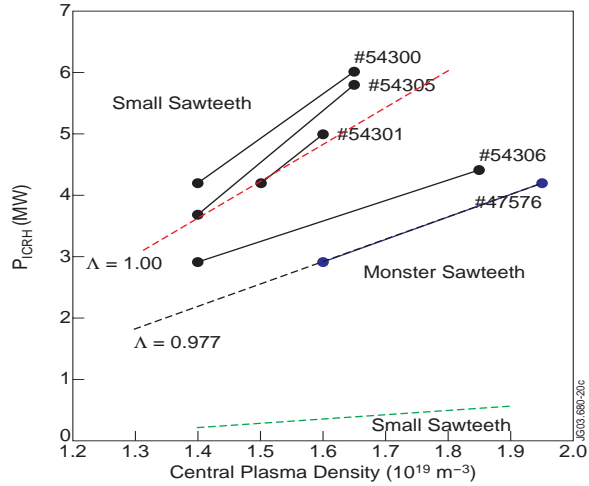


Figure 3.8 - Thresholds for sawtooth stabilization in the  $(n_e, P_{ICRH})$  plane for  $\Lambda=1.00$  (upper dashed line) and  $\Lambda=0.977$  (middle dashed line),  $n_{HOT}=1\%$  to  $5\%$ . The lower threshold is the same for both values of  $\Lambda$  and is represented by a green dashed line. Dashed lines represent the uncertainty in the exact location of the thresholds.

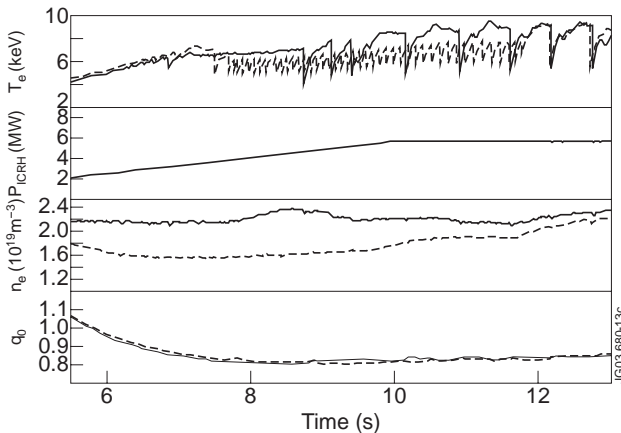


Figure 3.9 - Temporal evolution of the electronic temperature, ICRH total power input, central electron density and safety factor on the magnetic axis for pulses #47575 (solid) and #47576 (dotted).

The temporal evolution of sawtooth behaviour for pulse #47576 is represented in Figure 3.10, where the fast ions temperature threshold corresponds to a straight line in the plane  $(n_e, P_{ICRH})$ . In the reference discharge #47575 this threshold is never crossed and sawteeth are stable throughout the whole discharge.

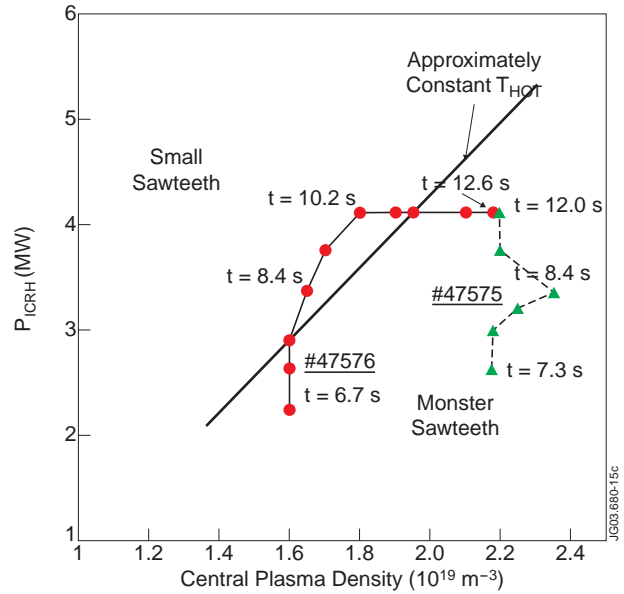


Figure 3.10 - Thresholds for efficient sawtooth stabilization by ICRH driven fast ions in pulses #47575 and #47576, with  $\Lambda=0.977$  and a minority ion concentration of  $1\%$ . These thresholds correspond to lines of approximately constant values of  $T_{HOT}$ . The values of  $P_{ICRH}$  indicated correspond to the values applied in  $t$ .

### 3.3.2.6. Sawtooth Stabilization During ICRH at Low Plasma Densities in JET

The stabilization of magneto hydrodynamic modes by high-energy fast particles is a question of fundamental relevance for future thermonuclear reactors. One common procedure to increase the fast particle population, in ion cyclotron heated (ICRH) discharges, is to operate with relatively low-density plasmas ( $n_e(0) < 2 \times 10^{19} \text{m}^{-3}$ ), which presented a new pattern of small scale and high frequency sawteeth (accompanied by a MHD activity with  $n = 1$  and  $f \approx 55 - 65 \text{ kHz}$ ). The occurrence of these sawteeth was attributed to decreasing stabilization effect of fast particles as their energy increases [section 3.3.2.5]. However, the density threshold between the two types of sawteeth seemed too sharp to be explained by this effect only. Therefore, a new experimental campaign was carried out to investigate whether other effects, such as runaway electrons, could provide a sharper distinction between these scenarios. The time evolution of relevant parameters of a low-density (controlled by gas puffing) discharge with large ICRH power is shown in Figure 3.11.

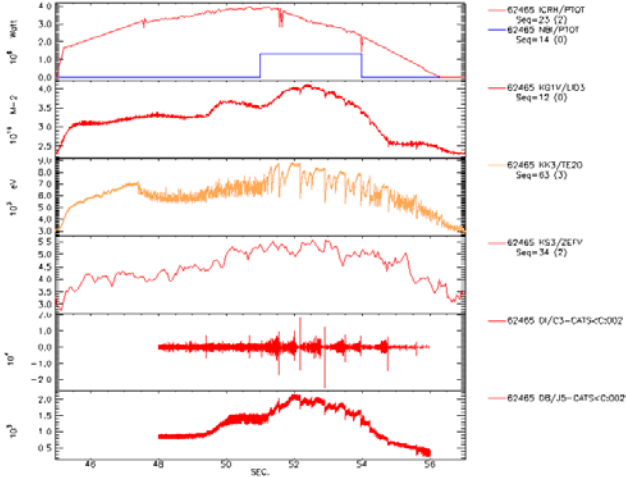


Fig 3.11 - Total ICRH and NBI powers, integrated central line density, electron temperature (measured at the ECE line-of-sight  $R = 3.18$  m), effective  $Z$ , Mirnov signal, and soft X-ray signal at the line-of-sight passing through the axis.

The phase of high frequency low-amplitude sawteeth, which are dubbed “grassy sawteeth”, starts at  $t \approx 47.5$  s and lasts up to  $t \approx 51$  s, when the NBI is turned on. At the end of the NBI pulse, at  $t \approx 54$  s, the density drops and the “grass sawteeth” return. The Mirnov signal shows some large spikes, which are not always associated with the sawtooth crashes.

There are two possibilities for a relevant role of runaway electrons on the sawtooth behaviour in these low-density discharges : (i) runaway electrons exist during the “grassy” sawtooth phase, at low density, and trigger some kind of instability that limits the duration of the sawteeth; (ii) a small population of runaways is present just during the large sawtooth period, stabilizing some mode inside the  $q = 1$  surface, which was causing the early sawtooth crash during the “grassy” period.

Let us assume that there is a stationary runaway electron population, due to balance between production and losses, somewhere at the beginning of the “grassy” sawtooth phase (at  $t = 48$  s), when this scenario is fully established. As the electron density and temperature vary, both the critical runaway energy and the runaway production rate  $S$  will change. Thus, we can get a qualitative information on the runaway population increase by calculating the ratio  $S(t)/S(t=48$  s), as the plasma density and heating power increase.

The results of a calculation, carried out for  $Z_{ef} = 4$  and the initial value of of the ratio of electric field to Dreicer field  $\alpha = 0.01$ , is shown in Figure 3.12. The initial value of  $\alpha$  was estimated from the values of the loop voltage on axis,  $V \approx 0.3$  V,  $n_e \approx 1.5 \times 10^{19} \text{ m}^{-3}$ , and  $T_e = 6$  keV, at  $t = 48$  s. It is clear that  $S$  increases substantially as the electron temperature increases, presenting large spikes that can

result in augmented runaway population, if the losses remain the same. We see that there can be a large runaway production at the end of the “grassy” phase as well as in the large sawtooth phase. Therefore, it seems unlikely that runways are playing a dominant role on differentiating the sawtooth behaviour between these phases.

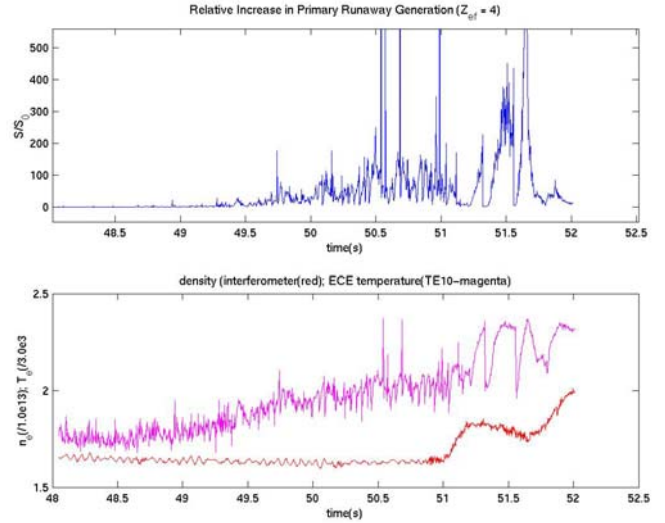


Figure 3.12 - Relative variation of the primary runaway production rate, with respect to that at  $t = 48$  s, and central electron density ( $n_e/10^{19} \text{ m}^{-3}$ ) (red) and temperature ( $T_e/3$  keV)(magenta), for discharge 62465.

### 3.3.2.7 Confinement effects of large islands

During the JET trace tritium campaign a set of discharges were produced with large magnetic islands induced by neo-classical tearing modes (NTM’s). Temporal measurements of the tritium rate of penetration observed by the 19 chord 14 MeV D-T neutron yield cameras indicate a possible correlation between the NTM and a reduction of the tritium particle confinement. To quantify the effects of NTM islands on the particle confinement time, transport studies have been started using TRANSP code.

A set of four trace tritium discharges, with and without NTM’s, has been modeled with TRANSP using the measured 14 MeV neutron emission to assess the quality of the modeling. Figure 3.13 presents the best matching obtained so far of the neutron emission evolution for the reference discharge of this study, one without NTM’s, for one vertical and horizontal chord. This case is determined minimizing the relative error between the experimental measured neutron emission and the calculated emission modeled by TRANSP. Figure 3.14 shows the results obtained using the minimization of the sum of the squared residuals method for the reference discharge when scanning in the diffusion coefficient. Results for the rise and decay phase of the tritium puff are plotted.

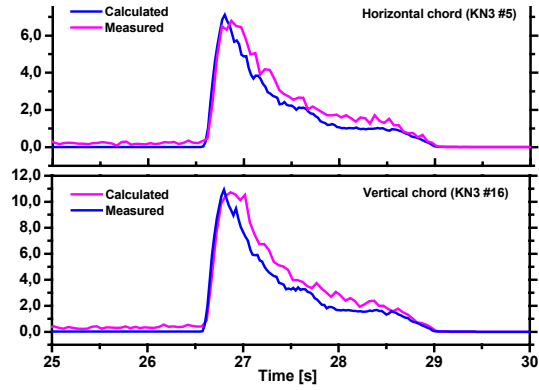


Figure 3.13 - Measured and calculated D-T 14MeV neutron emission along 2 chords during the Tritium puff.

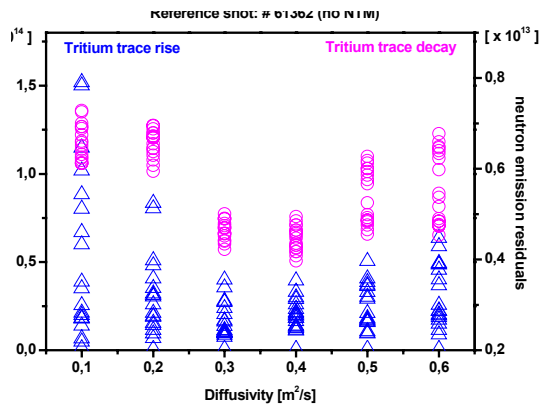


Figure 3.14 - Residuals from the minimization method used to assess the quality of the modelling and the best diffusivity that match the exp. data.

Preliminary analysis of the transport coefficients show that magnetic islands can affect the transport globally and not only locally as expected. Figure 3.15 depicts the non-diffusive pinch velocity for the tritium obtained in the rise phase of the tritium puff for discharges with and without NTM's (#61359 and #61362). In both cases, the particle diffusivity is the value which minimizes the relative error inferred from neutron emission chords as explained above and they are kept constant. Figure 3.16 shows the respective heat diffusivity for electrons and ions.

### 3.3.2.8 Effect on the fast particle population of externally induced error fields

The effect on the fast particle population of externally induced error fields locking to the  $q=2$  surface have been studied at JET. In the absence of radially resolved measurements of the fast ion distribution, the onset and the disappearance of Alfvén Eigenmodes (AEs) localised at different radial positions can then be used to provide evidence for the fast ion redistribution.

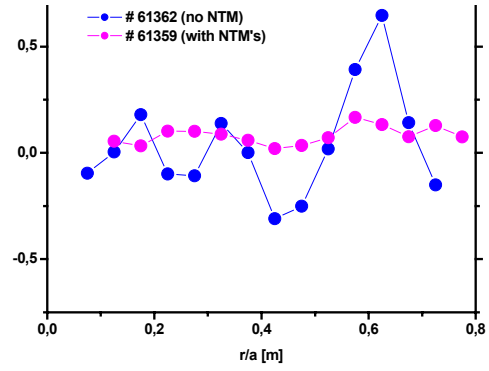


Figure 3.15 - Tritium pinch velocity for two discharges for a given particle diffusivity. (Here  $D_T/D_D = 3/2$ ).

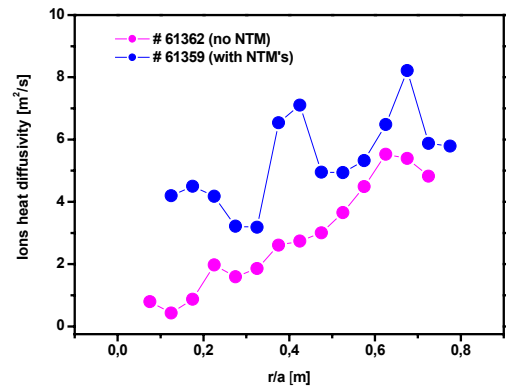


Figure 3.16 - Ion heat diffusivity for a discharge with and without NTM's.

Without externally applied error fields, the  $n=4$  Toroidicity induced Alfvén Eigenmode (TAE) becomes unstable at  $P_{ICRH} > 3$  MW, (Figure 3.17) and during the Ion Cyclotron Resonant Heating (ICRH) flat top phase reaches the amplitude at the plasma edge of  $|\delta B|_{TAE} > 1.3 \times 10^{-5}$  T. The  $n=4$  TAE is not observed when an island induced by the external applied error fields is present in the plasma, indicating that the destabilisation threshold is larger than  $P_{ICRH} > 4$  MW.

The difference observed for the  $n=4$  Ellipticity induced Alfvén Eigenmode (EAE) is a higher excitation threshold  $P_{ICRH} > 2$  MW with error fields, compared to  $P_{ICRH} > 1.1$  MW without error fields, thus indicating that a larger drive is required in this case (Figure 3.18). During the ICRH flat top phase, the mode reaches in both cases the amplitude at the plasma edge of  $|\delta B|_{TAE} > 1.4 \times 10^{-5}$  T. These results show that significant re-distribution of the fast ions take place when a magnetic island is present in the plasma.

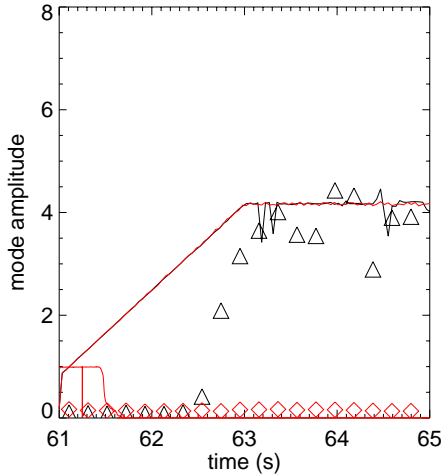


Figure 3.17 - Measured mode amplitude (a.u.) of the  $n=4$  Toroidicity induced Alfvén Eigenmode (TAE) as a function of time, without applied error fields (triangles) and with applied error fields (diamonds). The ICRH power (MW) is shown for comparison.

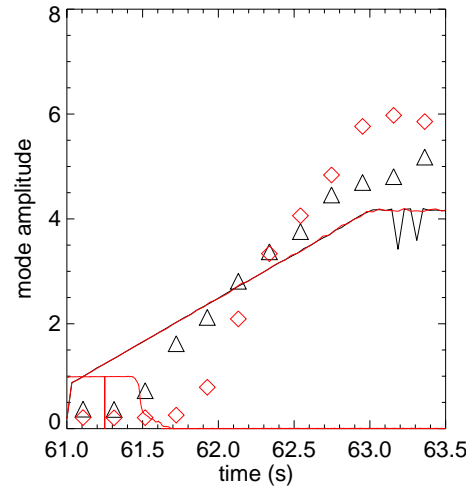


Figure 3.18 - Measured mode amplitude (a.u.) of the  $n=4$  Ellipticity induced Alfvén Eigenmode (EAE) as a function of time, without applied error fields (triangles) and with applied error fields (diamonds). The ICRH power (MW) is shown for comparison.

### 3.3.2.9. Studies on Density Limit Disruptions

Previous studies of density limit disruptions in small and medium size tokamaks found that degradation of the plasma energy confinement, characterizing major density limit disruptions, initiates in the neighbourhood of the  $m/n=2/1$  island. A flattening of the electron temperature profile was observed spreading inwards, to the center of the plasma, from the outboard O-point of the  $2/1$  mode. This sequence of events is also observed in JET density limit disruptions. Nonetheless these disruptions show features common to precursors and postcursors of other JET density limit disruptions, where Ne gas puff is used to provoke the disruption.

Low elongation limiter ohmic plasmas with  $n_e \text{ max} \sim 5 \times 10^{19} \text{ m}^{-3}$ ,  $q_a \sim 3.8$ ,  $I_p = 2 \text{ MA}$ ,  $B_t = 3 \text{ T}$  were used in these experiments. The electron temperature profiles were measured with  $100 \mu\text{s}$  time resolution (with a 96 channels ECE radiometer). The evolution of density fluctuations was measured from the low field side (LFS) with a fixed frequency, X mode, reflectometer at  $76 \text{ GHz}$  with  $1 \mu\text{s}$  time resolution. Both diagnostics are at the same toroidal phase of discharge #56953. Figures 3.19 and 3.20 refer to the energy quench phase of discharge #56953.

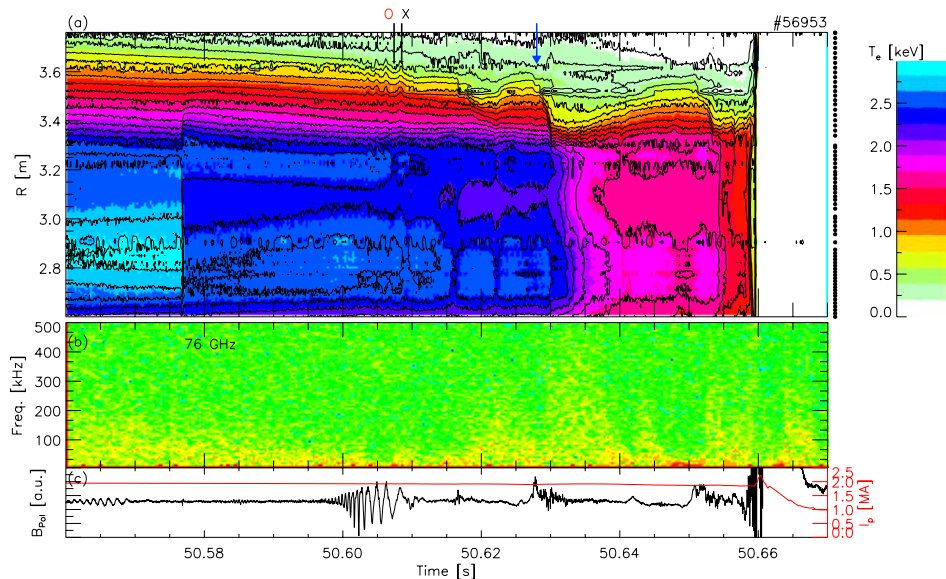


Figure 3.19 - Synchronized time evolution, during disruption, of (a)  $T_e$  measured with ECE radiometry. Dots at right indicate channels positions. (b) Spectrogram of fluctuations from  $76 \text{ GHz}$  X mode LFS reflectometer channel. The blue arrow in (a) indicates position of cut-off layer. (c) Perturbed poloidal magnetic field measured inside the vessel at the LFS and plasma current.

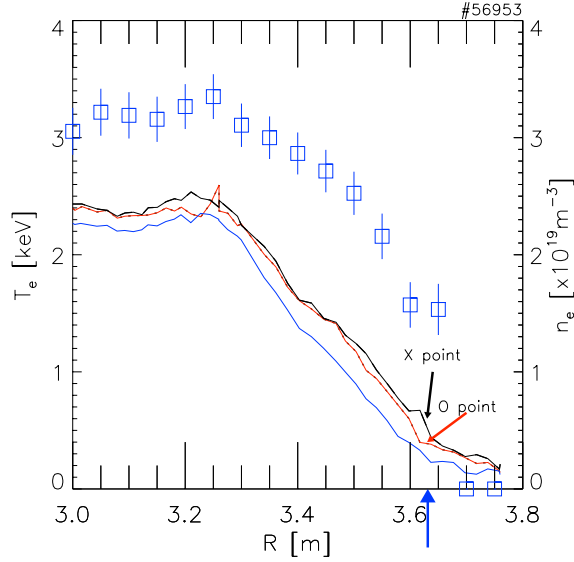


Figure 3.20 -  $T_e$  ECE profiles (lines) and  $n_e$  LIDAR profile (squares). Profiles in blue were measured at 50.6276 s. In red and black at 50.6074 s and 50.6085 s, respectively (see black arrows in Fig.3(a)). The red and black  $T_e$  profiles are shown to indicate the radius of the  $m/n=2/1$  island. Just like in Fig.3(a) the blue arrow indicates the position of the 76 GHz cut-off layer.

An abrupt increase of the frequency of the 76 GHz X mode fluctuations occurs at the onset of every disruption. Connecting this with the fact that the evolution of the  $T_e$  profiles measured in these three distinct size tokamaks by the common technique of ECE radiometry, shows the similar features described before, one can conjecture that electron density fluctuations in the neighbourhood of the  $m/n=2/1$  island are involved in the onset of the fast destruction of energy confinement in tokamak plasmas. Further measurements at JET of fluctuations at higher frequencies will allow clarification of the behaviour of these fluctuations deeper into the plasma core.

### 3.3.2.10. Investigation of the runaway electrons at disruptions in JET

A large number of major disruptions in JET has been analyzed to further understanding of the trends of disruption induced runaway process. Runaway generation has been observed in disruptions that occurred in a wide variety of different experimental conditions, namely, various triangularities and elongations, current rise stage, gas puff, Vertical Displacement Event (VDE).

It is found that runaway electrons have been better confined at higher toroidal magnetic field values (Figure 3.21). Fairly linear dependencies of the runaway current plateau values on plasma current derivative (Figure 3.22):  $I_{pl}(t)/dt = -[1/\tau_r] I_{pl}(0) \exp(-t/\tau_r)$  and pre-disruptive plasma current are demonstrating that the trends of runaway generation process during the disruptions in JET have not been changed substantially after divertor installation. It is

established that the conversion efficiency of the plasma thermal currents into runaway ones before and after divertor installation is remaining about  $\sim 42\% - 45\%$ . The trends described above show that runaway electrons might be an issue for ITER (high plasma currents and magnetic fields) and therefore it remains prudent to develop the disruption mitigation techniques, which ameliorate them and techniques to minimize halo currents, as well as prediction algorithms.

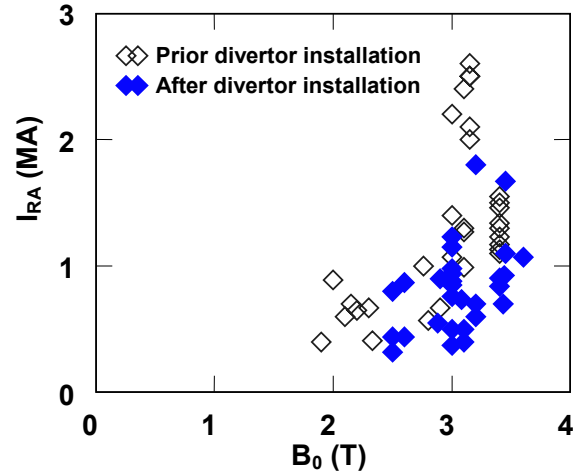


Figure 3.21 - Dependence of runaway current plateau values on toroidal magnetic field in experiments prior and after divertor installation.

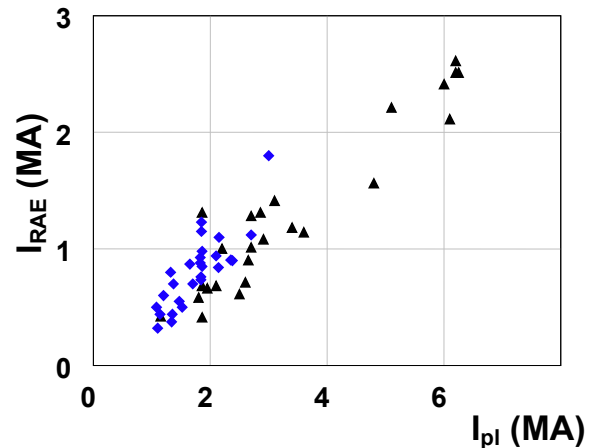


Figure 3.22 - Dependencies of runaway current values on plasma current derivative at the quench stage prior (grey stars) and after (blue diamonds) divertor installation.

Further runaway studies focused on the determination of the properties of magnetic configuration evolution during disruptions. Numerical modeling of the runaway generation during the disruption thermal quench has demonstrated that runaway electrons with substantial values of density and energy (up to  $10^{12}-10^{13} \text{ m}^{-3}$  and 10 MeV) can be generated during the thermal collapse in JET

disruptions, providing the initial conditions for further secondary runaway avalanching. The primary runaway electrons and their confinement at strong re-arrangement of the magnetic configuration during disruption play an important role for further avalanching which becomes the dominating process at the current quench stage. This has been investigated at JET.

Figure 3.23 presents typical example of the disruptions in discharges #54047 ( $B_0=3$  T,  $I_{pl}=1.9$  MA) and #54048 ( $B_0=3$  T,  $I_{pl}=1.9$  MA). These discharges disrupted under density limit conditions due to intense argon (54047) and helium (54048) puff. Disruption in pulse #54048 didn't cause observable runaway generation process, while all characteristic features of the runaway process including current plateau ( $I_{RA}\sim 0.9$  MA in #54047) and intense bursts of the hard X-rays and neutron emissions are presented in 3.23.

The estimates of the runaway electron energy have been carried out from the measurements of scattered  $\gamma$ -ray radiation with 250 and 300 ms time-bin integration. The spectra of scattered hard X ray emission were analyzed and evaluated energies  $E_\gamma$  have been taken as a low-limits for the runaway electron energy. Neutron blips (Figure 3.28) are the direct evidence that runaway electrons possess the energy  $E_\gamma > 11$  MeV if these neutrons are the result from  $Fe(\gamma,n)$ -reaction, or, even,  $E_\gamma > 19$  MeV, if  $^{12}C(\gamma,n)$ -reaction is the main neutron source.

Inverse reconstruction of the soft X-ray emission during disruption has been used to highlight the magnetic flux geometry evolution during disruptions. Figures 3.24 and 3.25 present the sequences of the reconstructed soft X ray images of the disruptions in pulses #54047 and #54048.

The soft X-ray images evolution during disruptions revealed that an axis-symmetric confining configuration has been created again in a very short time-scale ( $\sim 200$  microseconds) after reconnection of the magnetic flux and abrupt loss of the plasma energy. In #54047 (argon puff) the formation of the cold core has been followed by characteristic runaway current plateau, while the runaways at the disruption in #54048 (helium puff), have not been observed. Helium puff provides the relatively high electron temperature ( $T_e \sim 100$  eV) immediately at the beginning of the current quench phase. This temperature values are not low enough to provide the high electric field increase due to resistive effects and large plasma current derivative for creation of the stable runaway electron beam. Data is in an adequate agreement with the earlier observations made in JET disruptions prior to the divertor installation. It was shown that the probability of the runaway electrons generation in beryllium-bounded disruptions was significantly lower in comparison to that in carbon-bounded cases due to higher electron temperature immediately before the plasma current quench, i.e. carbon release during disruptions caused much stronger cooling effect in comparison to beryllium.

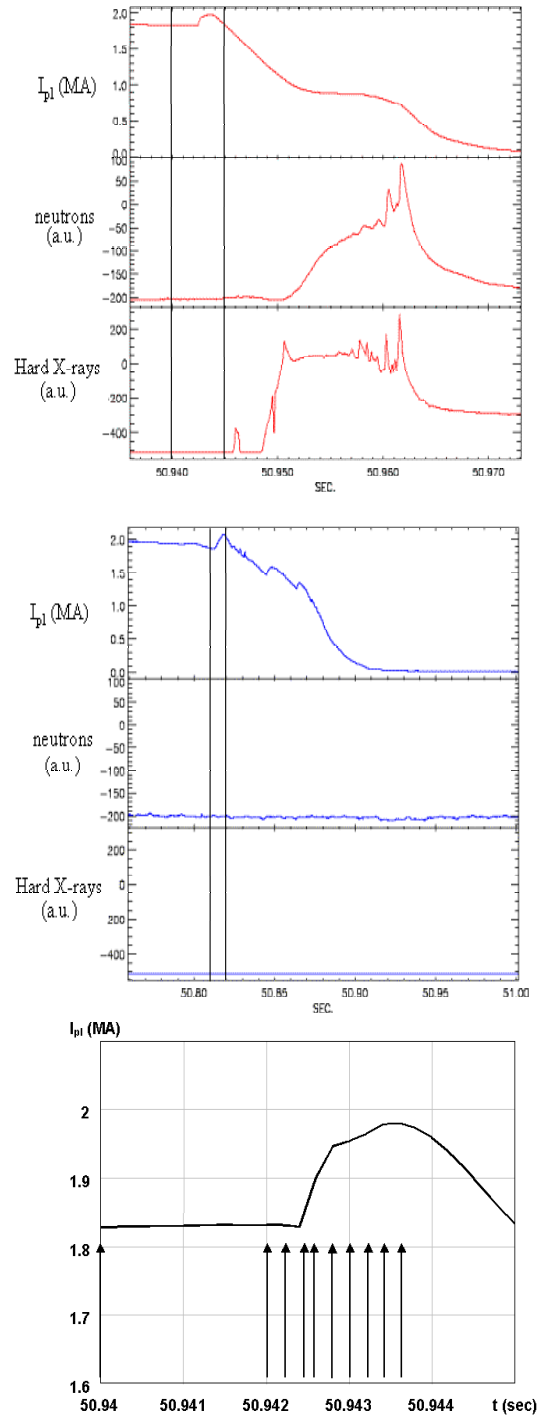


Figure 3.23 - Density limit disruptions in pulses #54047 (chart A) and #54048 (chart B). Soft X ray tomography has been used for reconstruction of the magnetic flux re-arrangement during disruptions. Reconstruction has been performed in temporal points marked by arrows in pulse #54047 (chart C) and within the temporal stage marked by vertical lines for pulse #54048 at the 100  $\mu$ sec interval.

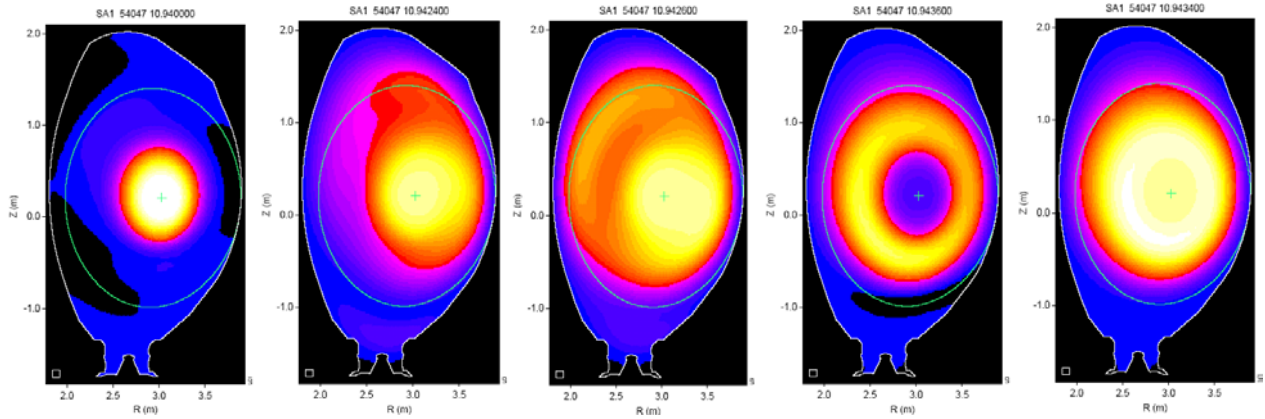


Figure 3.24 - Soft X-ray image of the disruption in pulse #54047. Intensity of soft X-ray emission is shown in arbitrary units.

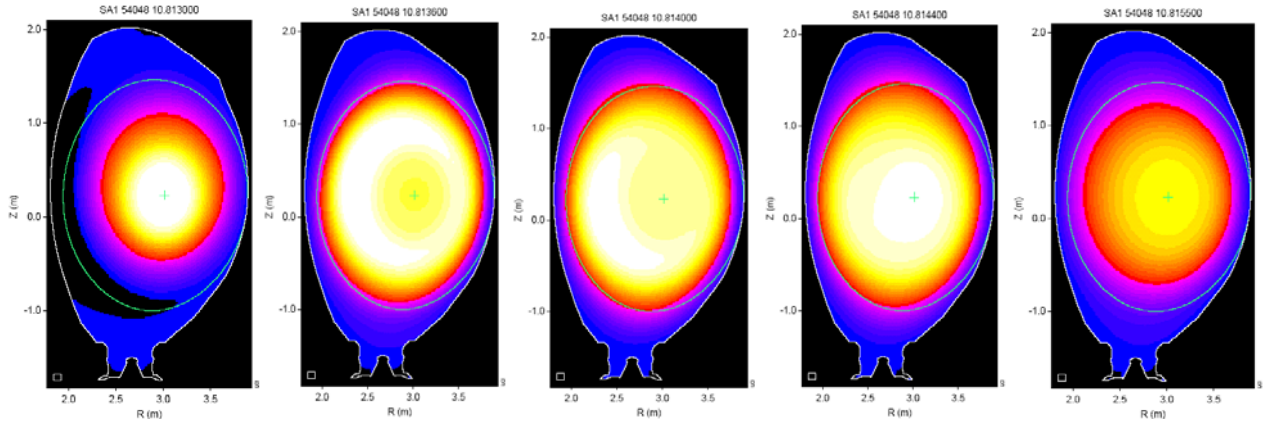


Figure 3.25 - Soft X-ray inverse reconstruction of the disruption in pulse #54048

### 3.3.2.11 Investigation of slowly rotating islands in JET discharges

One of the major questions related to the evolution of neoclassical tearing modes (NTM) is the critical value of  $\beta_{pol}$  necessary to trigger the mode unstable, starting from a stationary seed island. The marginal value of this parameter was investigated for the  $m/n = 2/1$  NTM in power ramp-down experiments in JET, at low values of the magnetic field and plasma current. The main parameters of a typical discharge in that campaign are shown Figure 3.26.

In spite of the large NBI power, the plasma rotates quite slowly in this discharge,  $f_{rot} \approx 1$  kHz, due to the effect of cyclotron waves on plasma rotation [M.J. Mantsinen et al., 2003]. Because of the low value of the toroidal field,  $B_t = 1.4$  T, only the ECE signals at the high-field side of the magnetic axis are available, so that the central electron temperature is not directly known. Nevertheless, large fluctuations in the electron temperature are observed in practically all the ECE signals, starting at  $t \approx 62.4$  s, as seen in the TE68N. In order to explain these oscillations in the

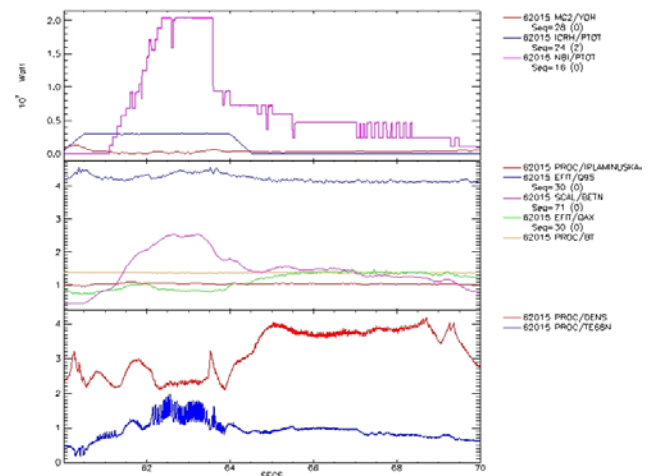


Figure 3.26 - Ohmic (YOH), ICRH, and NBI total powers,  $q_{95}$  (Q95),  $q_0$  (QAX), plasma current in MA (IPLAMINUKA), normalized beta (BETN), toroidal field (T) (BT), line average density (DENS), and electron temperature (keV) at  $R = 2.33$  m, for discharge 62015.

ECE signals, we have analysed the slow time evolution of them together with the MHD and central soft X-ray signals (Figure 3.27).

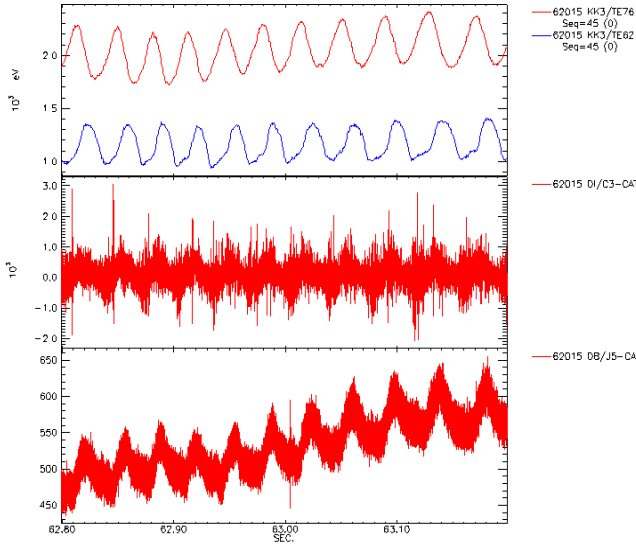


Figure 3.27 - Signals from two ECE channels, Mirnov coil, and central soft X-ray camera.

These signals show quite clear that there is a mode rotating steadily with a rather low frequency,  $f \approx 30\text{Hz}$ , in spite of the large momentum input by the NBI. This corresponds to a quite large  $m/n = 2/1$  island, as can be seen from the temperature fluctuations shown in Figure 3.28, rotating in the electron diamagnetic sense. It is possible that this slow rotation results from a balance between the diamagnetic effect and bulk plasma rotation. The central soft X-ray signal shown in Figure 3.27 suggests that an  $m = 1$  mode is also present, coupled with the  $2/1$  island.

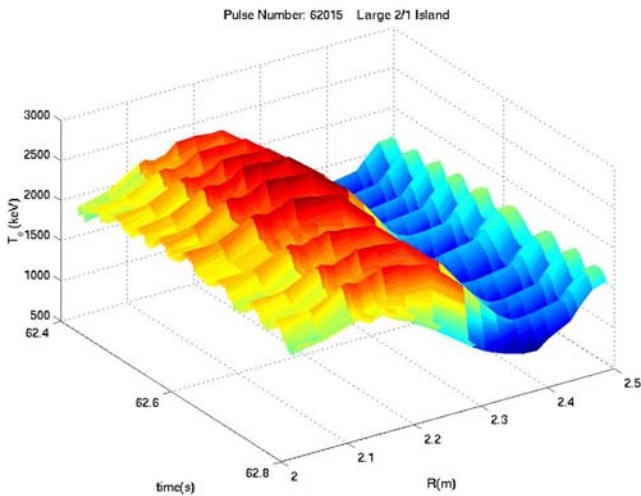


Figure 3.28 - Slow temperature oscillations associated with a large  $m/n = 2/1$  island in discharge 62015.

Therefore, it may be that the slow rotation corresponds to a steady-state solution of the momentum balance equation, including central momentum dissipation (as observed in ohmic discharges in TEXTOR).

### 3.3.2.12 Application of the Choi-Williams distribution to the time-frequency analysis of phenomena in fusion plasmas: precursors of edge localized modes and washboard modes

Given its good time-frequency resolution, the Choi-Williams distribution can identify fast precursors of MHD instabilities such as ELMs, or resolve events occurring closely in time, such as the rapid interaction between ELM precursors and washboard (WB) modes.

ELM precursors Figure 3.29 (a) shows an electron cyclotron emission (ECE) signal in which, in conjunction with the  $D\alpha$  signal that is also shown, it is possible to identify an ELM precursor with frequency around 50 kHz. As the precursor only lasts about 0.2 ms, the spectrogram is unable to resolve it. As seen in (b), done with a time resolution of  $\delta t_p = 0.25\text{ms}$ , just about the expected duration of the precursor, the frequency resolution of the spectrogram is already insufficient to yield a clear picture. The result of applying the Choi-Williams distribution to this signal can be seen in figure (c). The time resolution is  $\delta t_{CW} = 0.1\text{ms}$ . The precursor is clearly shown at 50 kHz, and other low frequency modes that exist in the signal can be seen as well.

Washboard modes WB modes have been seen to interact with ELM precursors, in a way suggesting that both phenomena cannot happen at the same time. Time-frequency mode-number plots, which, like the spectrogram, are based on short-time Fourier analysis, have been presented to demonstrate this behaviour. In such plots, WB modes are seen as several broad frequency bands of magnetic fluctuations, not having well-defined frequencies. Here, a magnetic signal is analysed where it is possible to see this interaction between a type-I ELM precursor at 15 kHz and WB modes between 25 kHz and 50 kHz. Signal components below 13 kHz have been removed by filtering to provide clearer pictures. Figure 3.35(a) shows a spectrogram with time resolution  $\delta t_p = 0.5\text{ms}$ , which allows seeing the intermittent ELM precursors and WB modes. Although the alternating appearance of the two mode types can be seen with the spectrogram, the trade-off between time and frequency resolution limits the sharpness of the time-frequency representation. A clearer time-frequency picture is achieved with the Choi-Williams distribution, as shown in Figure 3.35(b), where a better frequency resolution is achieved with the same time resolution of the above spectrogram,  $\delta t_{CW} = 0.5\text{ms}$ .

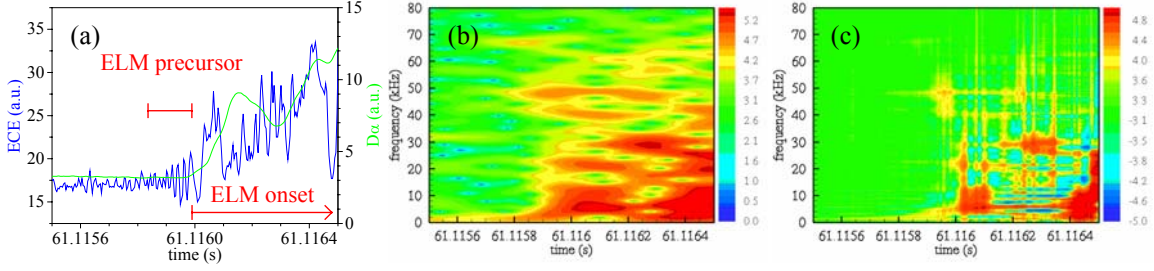


Figure 3.29 - In (a) edge ECE and  $D\alpha$  signals (JET pulse 53060) reveal the presence of an ELM precursor between 61.1158 s and 61.1160 s, with a frequency of about 50 kHz. The ECE signal has been analysed using (b) the spectrogram, and (c) the Choi-Williams distribution.

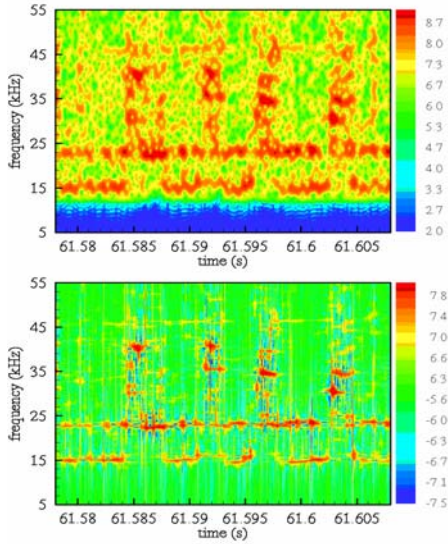


Figure 3.30. Analysis of a magnetic pick-up coil signal (JET pulse 55976), using (a) the spectrogram, and (b) the Choi-Williams distribution. The interruption of the WB modes by the type-I ELM precursor is best seen with the Choi-Williams distribution.

### 3.3.3. Work within Task Force D plus support to E, M and S<sub>1</sub>

#### 3.3.3.1. Combined mass-energy analyzer for the investigations of SOL plasmas.

Traditional spectroscopic impurity diagnostic allows observing the spatial distributions of high charge state impurities in the main plasma, and the influx of low charge states near the boundary. Very limited diagnostic techniques are available for the study of the flux and charge state distribution of impurities and plasma ions in the tokamak SOL plasma. Mass spectroscopy existing technique exploits the local magnetic field of the plasma device, and the ion selectivity is based on the mass dependence of the  $E \times B$  cross-field drift of ions (plasma ion mass spectrometer (PIMS) and Omegatron ion mass spectrometer). The technique considered here is based on a

Bennett-type mass-spectrometer (BTMS), which presents a non-magnetic mass spectrometer with axial RF field.

In the simplest (one-stage) case the instrument consists on axial sequence of the grids ( $G_1, G_2, G_3, G_4$ ) and collector. The ions are accelerated up to some potential  $U$  applied between grids  $G_1$  and  $G_2$ . The RF stage is formed by grids  $G_2$ - $G_3$ - $G_4$ , where the additional energy  $\Delta W$  is acquired by the ion. This additional energy is maximal at some conditions, and if the retarding potential,  $U_R \geq U$ , is applied between the grid  $G_4$  and collector, then the ions with one particular  $M/Z$  will be collected in accordance with  $M[\text{amu}]/Z = 0.266 U[\text{V}] / (s^2[\text{cm}]^2 [\text{MHz}])$ , where  $s$  is the spacing between the grids  $G_2$ - $G_3$  and  $G_3$ - $G_4$ , and  $f$  is the RF field frequency. The resolution can be increased by multiplication of the number of RF stages.

The advantages of using BTMS in a fusion plasma by comparison with PIMS and Omegatron probes are namely: i) no dependence on magnetic field value; ii) simplicity in operational principle and construction; and iii) natural possibility to work as a retarding field energy analyzer (RFA) which spreads the capabilities of the instrument in general. The last one suggested the possibility of operation of the already existing RFA at JET as a BTMS.

The preliminary considerations were done on the examples of  $^{12}\text{C}^{+4}$ ,  $^{12}\text{C}^{+3}$ , and  $^2\text{D}^{+1}$  ion species, and include the resolution and current efficiency estimations. The resolution and current efficiency of BTMS have been obtained by plotting the percentage of maximum energy gain,  $\Delta W / (\Delta W)_{\text{max}}$ , an ion receives at the exit of the RF stage, versus the RF phase angle,  $\theta$ , at the entrance. The current efficiency can be calculated by  $I/I_0 = \Delta\theta/\pi$ , where  $\Delta\theta$  is the “interval of transparency”, or the interval of phase angles above the mass-resolving discrimination level.

For the cases considered the estimated current efficiencies are shown in Table 3.2.

Ion specie	$^2\text{D}^{+1}$	$^{12}\text{C}^{+3}$	$^{12}\text{C}^{+4}$
Discr. Level	0.94	0.87	0.61
Current efficiency	0.23	0.32	0.58

Table 3.2 – Current efficiencies and discrimination levels for each considered ion species

Taking the distance between the grids the same as JET RFA,  $s=0.2$  cm, obtain the operational parameters shown in Table 3.3 for two-stage BTMS.

Ion specie	${}^2\text{D}^{+1}$	${}^{12}\text{C}^{+3}$	${}^{12}\text{C}^{+4}$
$U_s$ , V	48	16	12
$U_r$ , V	480	160	120
$U_R$ , V	550	230	190
Res. Freq., MHz	40	18.8	16.3

Table 3.3 – Operational parameters for each ion species

Further work with numerical simulations to specify exactly the combined RFA-BTMS in conditions close to the real plasma experiment is necessary.

### 3.3.3.2. Probability density function of the radial structure of turbulence in fusion plasmas

Plasma profiles and turbulence have been investigated in the JET plasma boundary region using a fast reciprocating Langmuir probe system located on the top of the device. The Probability Density Function (PDF) of the effective radial velocity and radial scale of turbulent events was used as a strategy to identify the underlying physics of anomalous diffusivities and inward velocities.

The plasmas studied were produced in X-point plasma configurations with toroidal magnetic fields  $B = 1 - 2.5$  T,  $I_p = 1 - 2$  MA (ohmic plasmas) in the JET tokamak. The local time resolved radial ExB turbulent induced fluxes,  $\tilde{\Gamma}(t) \propto \langle \tilde{n}(t) \tilde{E}_\theta(t) \rangle / B$ , (where  $\tilde{n}$  and  $\tilde{E}_\theta$  are the fluctuating density and poloidal electric field, respectively) were calculated neglecting the influence of electron temperature from the correlation between poloidal electric fields and density fluctuations. An effective radial velocity has been defined as the normalized ExB turbulent particle transport to the local density,  $v_{eff} = \langle \tilde{I}_s \tilde{E}_\theta \rangle / I_s B_T$  where  $I_s$  is the ion saturation current. The statistical properties of the radial coherence of fluctuations and transport have been computed from the cross correlation of  $\Gamma_{ExB}$  signals and floating potential signals radially separated 0.5 cm.

Figure 3.31 shows the measured ion saturation and floating potential profiles in plasmas in which the reciprocating probe was radially shifted shot by shot from the Scrape-Off-Layer (SOL) up to the velocity shear layer location. The reproducibility in the measured radial profiles is very good.

Figures 3.32 and 3.33 show the PDF of the radial coherence of fluctuations and transport.

In Figure 3.33, the PDF of the radial coherence of ExB transport shows tails (i.e. sporadic events with high radial coherence). PDFs of the radial coherence of fluctuations are wider than those corresponding to the ExB turbulent flux. Furthermore, tails in radial-PDFs are modified in the presence of sheared poloidal flows in the plasma boundary

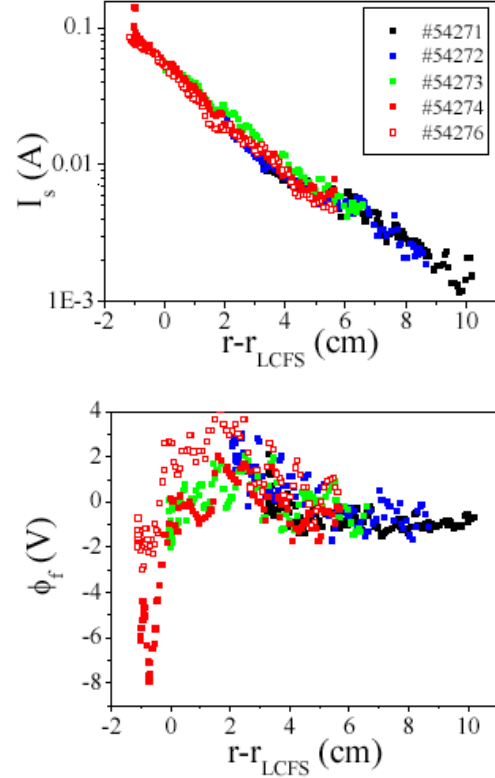


Figure 3.31 - Radial profiles of ion saturation current and floating potential in the JET boundary region (ohmic plasmas) in reproducible discharges.

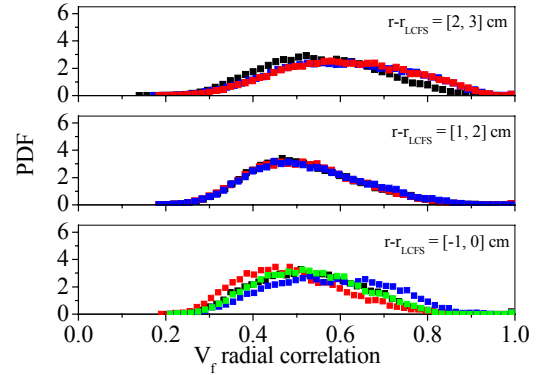


Figure 3.32 - PDFs of the radial correlation of the floating potential fluctuations in the JET boundary region.

region. Far from the shear layer the radial correlation of the fluctuations exhibits a wide PDF that covers a large range of radial scales. When approaching the shear layer the PDF becomes narrow. These results can be interpreted on the basis of the influence of sheared flows on the radial scale of fluctuations and transport.

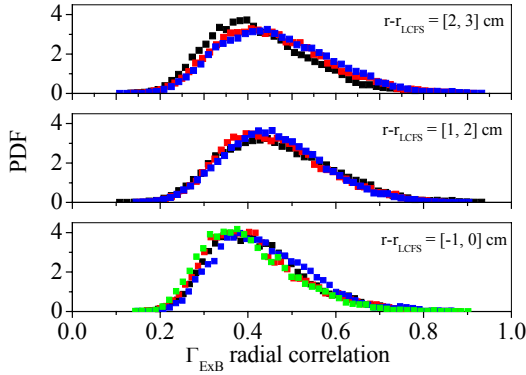


Figure 3.33 - PDFs of the radial coherence of ExB transport in the JET boundary region.

Figure 3.34 shows  $v_{\text{eff}}$ -PDFs. In the SOL region  $v_{\text{eff}}$ -PDFs show clear non-gaussian features with both positive (radially outwards transport) and negative (radially inwards transport) events. Although the most probable radial velocity is in the order of 10 m/s, experimental evidence of intermittent events propagating radially with velocities in the range of 100–400 m/s is clearly observed, in agreement with previous experiments. This result illustrates the presence of large and sporadic transport (velocity) events.

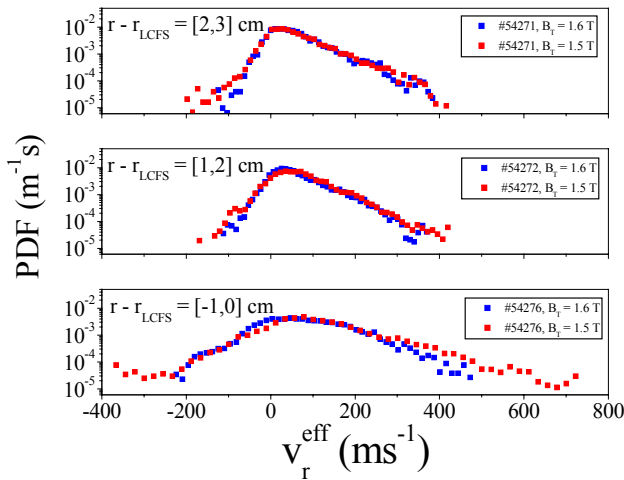


Figure 3.34 - PDFs of radial effective velocity in the JET plasma boundary region.

A clear modification in  $v_{\text{eff}}$ -PDFs takes place near the shear location:  $v_{\text{eff}}$ -PDFs become broader and more gaussian and about 20% of the particles move radially inwards with averaged radial velocities of about 50 m/s.

### 3.3.3.3. Determination of the particle and energy fluxes in the far SOL during ELMs using the Reciprocating Probe diagnostic

In between ELMs most of the energy transported across the separatrix onto the SOL plasma is deposited in the divertor

targets. However, there are indications that during ELMs a significant part of the energy may be deposited outside the divertor region. Reciprocating probe data show that the far SOL particle flux strongly increases during ELMs. In terms of divertor power loads, this observation is only relevant if associated with the high particle flux to the wall there is also a significant heat flux. The temperature time evolution was therefore measured to investigate the heat flux in the JET far SOL during ELMs.

ELMs propagate radially with velocities up to 1 km/s, so that the ELMs arrival time to the plasma wall can be comparable to the characteristic time of transport to the divertor. Furthermore, both the particle flux and the effective radial velocity in the far SOL decrease as the ELM frequency increases (Figure 3.35). Since the low frequency ELMs lead to larger energy losses, results suggest that the radial velocity (as well as the particle flux in the far SOL) depend on the ELM energy loss.

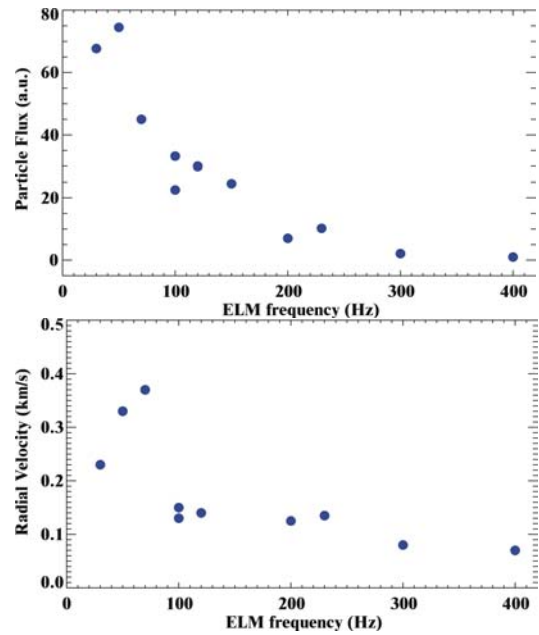


Figure 3.35 - Dependence of the particle flux and radial velocity on the ELM frequency.

The electron temperature ( $T_e$ ) has been estimated using a modified triple probe method and results indicate that  $T_e$  increases by a factor of 2-3 for large ELMs (frequency between 50-100 Hz). The resulting heat flux ( $q_{\parallel} = \gamma T_e J_{\text{sat}}$ ) in the far SOL increases by a factor of  $\sim 10$  during an ELM, being that increase mainly due to a rise in the local density. The radial particle and heat fluxes induced by fluctuations have also been estimated during ELMs (Figure 3.36).

Assuming poloidal symmetry, the total electron energy to the far SOL has been estimated. During ELMs the energy carried by electrons to the far SOL is negligible,  $< 5\%$ .

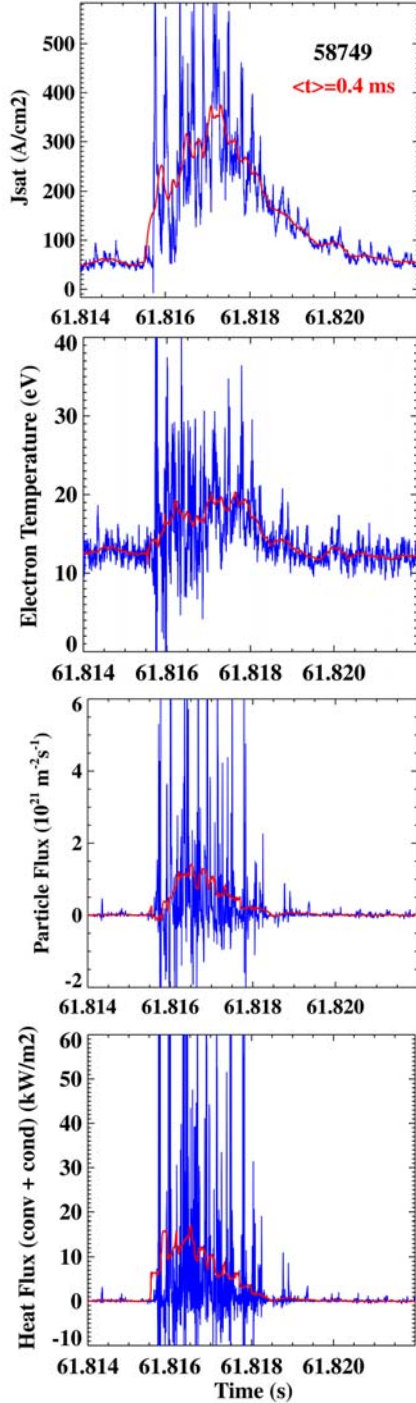


Figure 3.36 - Time evolution of  $J_{sat}$ ,  $T_e$ ,  $\Gamma_{ExB}$  and  $Q_{\perp}$  during an ELM (pulse 59749).

This result is in agreement with theoretical predictions, which show that electrons are rapidly cooled by parallel conduction to the divertor target. However, that should not be the case for ions, which may carry a significant energy to the far SOL.

### 3.3.3.4 Effect of toroidal field reversal on the SOL properties

Edge and SOL plasma parameters have been compared in plasmas with standard and reversed toroidal field directions. Based on classical effects (e.g. particle drifts) it is expected that the parallel flows in the SOL reverses with the reversal of the magnetic field direction. However, no evidence of symmetrical reversal in parallel flows has been observed, in agreement with previous findings. This asymmetry suggests that a mechanism is driving flows, which is independent of field direction. Turbulent transport driven flows is a clear candidate. We have observed that the basic turbulence properties (e.g., level of fluctuations, ExB transport) look rather similar in reversed and standard-B configurations. This suggests that turbulence driven flows are not significantly modified in reversed B-field. A combined role of both plasma flows driven by drift effects and turbulent transport mechanisms can explain JET experimental findings.

### 3.3.3.5 ELMs studies with microwave reflectometry

Some physical studies were performed from data analysis of both KG3 and KG8b reflectometers. In the experiments devoted to the “Quiescent H-mode” (QH-mode) regime, a MHD oscillation with up to 7 harmonics, similar to “Edge Harmonic Oscillation” (EHO), was observed during the ELM free phases with the KG8b data (Figure 3.37).

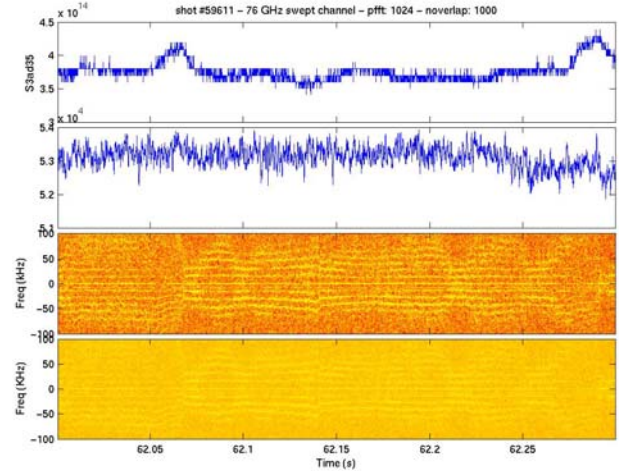


Figure 3.37 - Spectrogram of the KG8b reflectometer signal at 76 GHz illustrating the EHO during an ELM free phase in the QH-mode regime

Reflectometry measurements of Alfvén cascades have been obtained in JET with the KG3 O-mode reflectometer. This allowed an unprecedented clear observation of the temporal and spectral evolution of this kind of cascades (Figure 3.38). The originality of this result comes from the fact that it was obtained for a probing wave frequency higher than the plasma frequency (interferometer-like measurements).

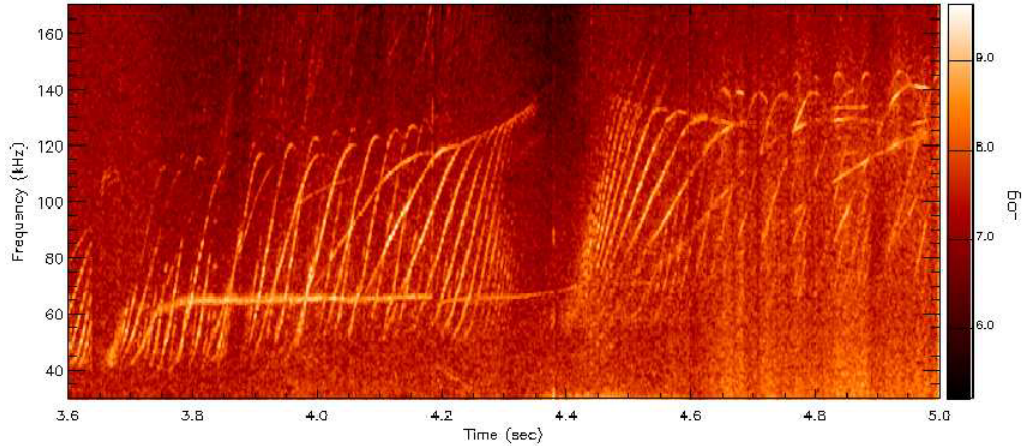


Figure 3.38 - Spectrogram of the KG3 reflectometer signal at 45.2 GHz depicting clearly the evolution of some Alfvén cascades

A study of the ELM activity using the KG8b reflectometer is in progress. The 76-78 GHz channels (which generally probe the plasma edge region) are quite sensitive to the ELM activity (Figure 3.39). A significant broadening of the turbulence spectrum and some low-frequency modes appear just before the ELMs.

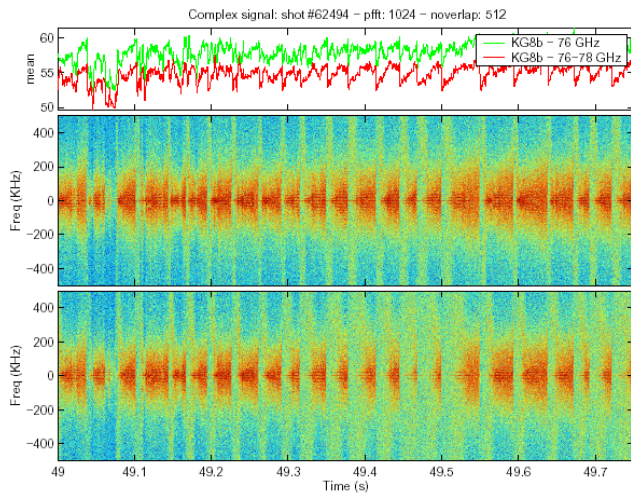


Figure 3.39 - Spectrogram of the 76 GHz and 76-78 GHz channel signals of KG8b in the presence of ELMs

We can also notice a strong effect of the ELMs on the amplitude and the phase of the reflected signals (Figure 3.40). The amplitude increases between two successive ELMs and drops down abruptly during the ELMs whereas the phase presents some plateaus between the ELMs and some jumps during the ELMs.

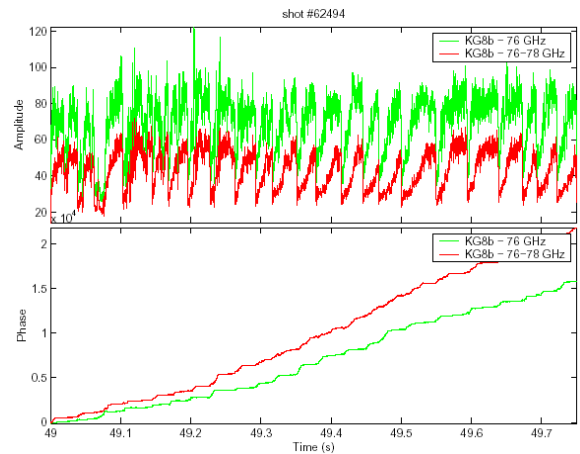


Figure 3.40 - Amplitude and phase (I and Q signals) of the 76 GHz, 76-78 GHz channel signals of KG8b in the presence of ELMs.

### 3.3.3.6. Plasma studies from MSE measurements

Studies were performed to assess the possibility to measure the on-axis density current  $J_0$  directly from motional Stark effect (MSE) data, during extreme reversed shear regimes where a so-called current hole is present. This technique has been previously reported from General Atomics [C. C. Petty, (2002)]. The main innovation in this technique is the use of second order polynomials instead of linear slopes to fit the MSE channels inside of the current hole. This is particularly important as the MSE profiles shows clearly that they are described by curves indicating a non-uniform rise of the current density in current hole regimes. Preliminary results showed an expected near zero current density during the time when the current hole was present.

Furthermore, the possibility to observe a small reversed current during the current hole, with this technique has been suggested despite the error bar for the measurement is still large. Efforts are under the way to reduce such large error bar to confirm whether or not the current goes negative in JET's extreme reversed shear plasmas.

### 3.4. JET ENHANCED PERFORMANCE PROJECT

#### 3.4.1. Introduction

The Association EURATOM/IST has been in charge with the tasks referred to in Table 3.4, in the frame of the JET – EP Project

Name	Frame
Mw Access – Project Management and Implementation	EFDA/01-625
Real-time diagnostic	Notification
FDA Project design and procurement activities	JW2-TA-EP-FDA-01
MPR Project design and procurement activities	JW3-OEP-IST-13
TOF Project design and procurement activities	JW3-OEP-IST-14
RTP Development real-time test facility	JW3-OEP-IST-15

Table 3.4 – Tasks concerning the JET-EP Project

#### 3.4.2. Millimeter wave Access (EFDA/01-625)

The MWA project aims at the installation of a new access for millimeter wave diagnostics on JET, consisting namely

in new antennas and waveguides for both reflectometry and ECE.

During 2003 this project had the participation of CFN-IST, IPP, FOM, CNR and CIEMAT (with L. Cupido as Project Leader). It was completed the design of all parts of the system and the consequent elaboration of specifications and contracts for manufacturing. The project was also modified to incorporate oblique view ECE antenna and waveguides. The main milestones during 2003 were the following:

- Vacuum window design. The study (by FOM) proposed a window based on a double window – double mirror design. Simulations of the performance where made and several enhancements were done to improve the performance, namely the inclusion of lossy dielectric filling the surrounding space. CFN-IST elaborated a mechanical design in conformance with JET vacuum requirement
- Global Antenna cluster design plus window. The designs and technical specifications were part of a call for tender during 2003 and actual selection of the proposals took place during this year. This part of the work needs to be ready to be installed during the 2004 shutdown. Effective manufacturing started by the end of 2003.
- The waveguide routes and their expected performance, based on the studies done during 2002 led to the full design of all parts for the transmission lines, namely the miter-bends and gap-joints (Figure 3.41).

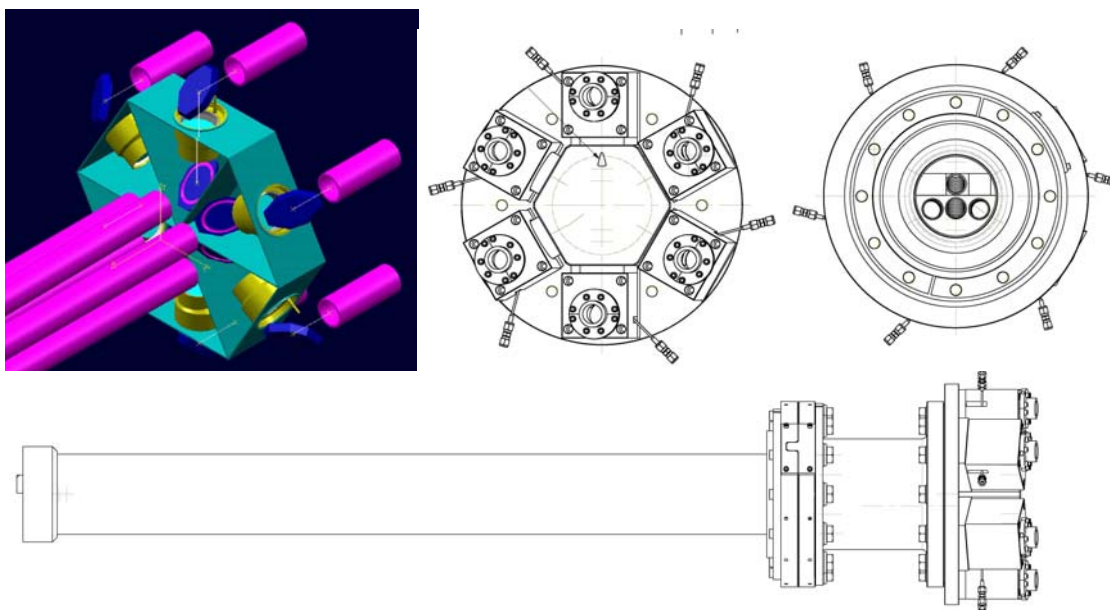


Figure 3.41 - Antenna cluster insert and vacuum window box.

### 3.4.3. Real-time implementation of the MSE diagnostic

The work aimed at data validation and making the motional Stark effect diagnostic (KS9RT) fully automatic in its operation, removing therefore superfluous human interaction as well as checking the time evolution of the front-end frequency response on data acquisition. Comparison of results between the real-time and off-line MSE systems were performed for various pulses, (Figure 3.42), showed a good agreement between both systems.

The toroidal magnetic field is now being read in real-time on the ATM Real Time Measurement and Control (RTMC) network in order to perform the Faraday correction on the calculated light polarization angle. This correction was previously done by supplying the real-time system with a reference pulse for taking the toroidal field data. The disadvantage was that every time the magnetic conditions changed, the user would have to supply a different reference pulse. With this new improvement, KS9RT is a fully automated diagnostic.

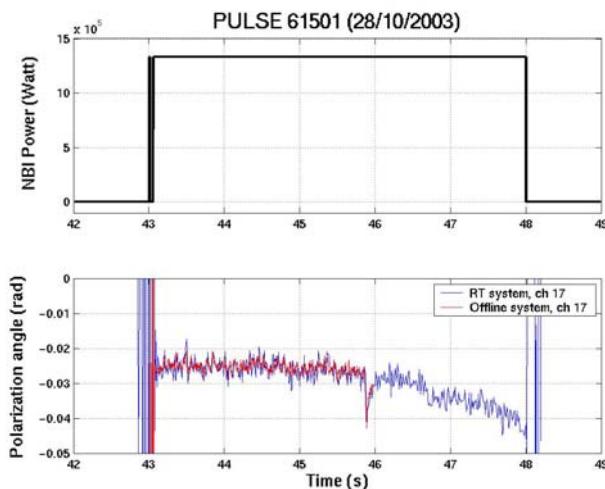


Figure 3.42 – Comparison of the results of the real-time and off-line MSE diagnostics

### 3.4.4. Fast ADC upgraded system for the heterodyne radiometer (kk3) diagnostic

The following main activities were carried out in 2003:

- Final testing of the system operation in the JET CODAS;
- Implementation and testing of a remote boot system;
- Development and configuration of software to support the insertion of a seventh transient recorder module.

### 3.4.5. Real-time test-bench

#### 3.4.5.1. Main activities

The following main activities were carried out:

- Conceptual design of the system;
- Elaboration of a proposal regarding the use of this system on the JET Real-time upgrade Phase 2;
- Discussion of this proposal with the EFDA Culham Close Support Unit;
- Beginning of the development of the PCI DAC modules.

#### 3.4.5.2. Module description

A test-bench which generates the stimulus signals for testing a real-time control system and simultaneously recording its output variables is being developed for the Real Time Project (RTP) of the JET. The RTP is an upgrade of the real-time capabilities of the JET measurement and control tools. The objective of the test-bench is to simulate the operation of a real-time control system by using as inputs the plasma variables previously stored on the JET pulse database or user defined through a graphical interface. This non-intrusive test method allows testing the control system for all possible operation scenarios without harming the real machine/system to be controlled.

The test-bench architecture (Figure 3.43) is based on a Real-Time Stimulus Generator (RTSG) device which provides up to 32 analog output channels to generate the analog stimulus for the system under test. Additionally the stimulus data can be transmitted through an ATM link for the measurement and control processors which have this type of interface. Up to 32 output variables from the system under test can be measured by a Real-Time Data Recorder (RTDR) for later analysis.

Data from previous JET pulses, user defined waveforms and recorded data are contained in an MDSplus database server and managed through a user interface elsewhere on a remote terminal over an Ethernet link. An HTTP server running on both RTSG and RTDR obtains a configuration from the CODAS Level 1 interface to setup its operation parameters such as pulse number, names of predefined waveforms and addition of noise.

### 3.4.6. Time digitizer and transient recorders for the neutron diagnostics enhancements

#### 3.4.6.1. Main activities

The following main activities were performed:

- Discussion of new data acquisition requirements of the diagnostic with the Project Leader;
- Design of the schematic, printed circuit board, programmable logic and control DSP firmware of both the PCI time digitizer and the PCI transient recorder modules;
- Assembling and testing of a prototype of each module.

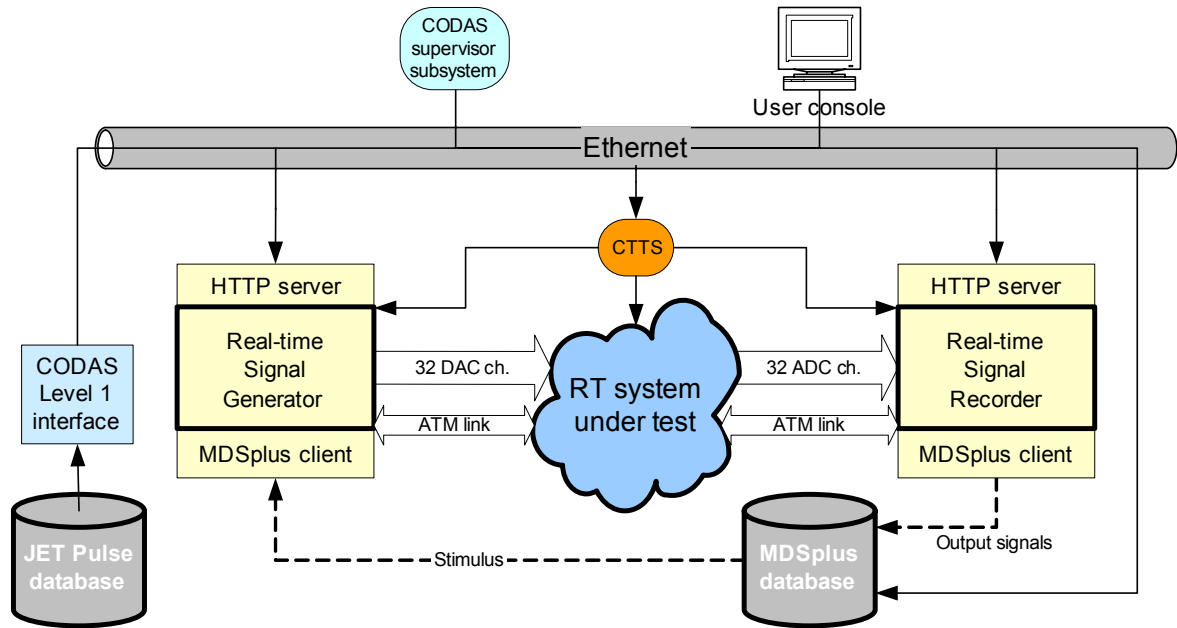


Figure 3.43 - Test-bench architecture

#### 3.4.6.2. Time digitizers

A PCI time digitizer module with eight Time-to-Digital Converter (TDC) channels is being developed for a time-of-flight spectrometer designed for optimized rate (TOFOR). The module shall measure, with high accuracy and resolution, flight-times of neutrons in the 100-ns range as provided by two groups of scintillation detectors operating at event (the occurrence of a neutron hitting the scintillator, tagged by the neutron arrival time value) rates up to several hundred kHz. The module stores up to 64 million hit-times with a resolution of 0.4 ns and incorporates a Digital Signal Processor and a System-On-Chip device which performs the data transfer, the device control/monitoring and may perform statistical, data reduction or control algorithms in real-time. TOFOR is a new instrument for 2.5-MeV neutrons to diagnose deuterium plasmas of the EFDA-JET tokamak with the high accuracy that comes with the ability to operate at event rates approaching the theoretical limit of the coincidence measurements.

#### 3.4.6.3. Transient recorders

A PCI transient recorder module is being developed as part of the upgrade of the magnetic proton recoil neutron (MPRu) spectrometer. The MPRu will use a 32-channel focal plane detector with laminated scintillators of so-called Phoswich type, each scintillator is read out by two PM tubes. The radiation-characteristic shape of the PM tube pulses is digitized and stored by the transient recorders for later analysis. The purpose of the new focal detector and accompanying electronics is increase the measurement sensitivity by many orders of magnitude compared with present system. The JET-EP project MPRu will allow 2.5-

and 14 MeV neutron emission spectrometry diagnosis of both D and DT and serves as a prototype test for ITER.

To attain the specific requirements of this diagnostic a 200 MSPS transient recorder with four independent Analog-to-Digital Converter (ADC) channels was designed. The hardware architecture proposed for the digitizer module is based on a PCI 2.2 board which includes a Texas Instruments® TMS320C64xx family Digital Signal Processor (DSP), a Xilinx® FPGA, an ADC front-end and up to 256 MB of SDRAM memory. With this architecture the maximum sustained pulse hit-rate in each channel is up to 1.25 MHz when digitizing 80 samples for pulses of up to 400 ns width. Figure 3.44 shows the transient recorder module hardware.

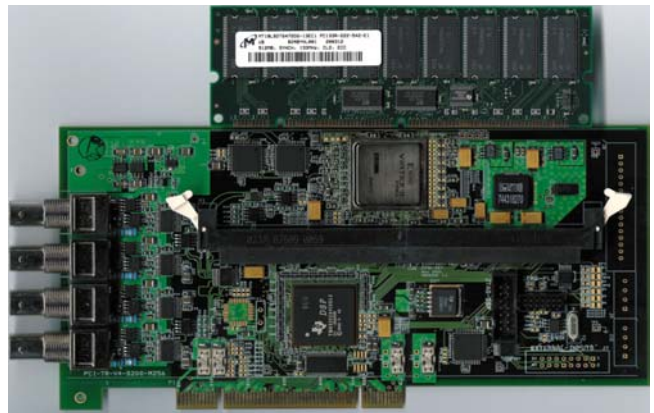


Figure 3.44 - Four channels 200 MSPS Transient recorder module

### **3.5. MANAGEMENT**

The Association EURATOM/IST has collaborated on the management of the use of the JET facilities by the EFDA Associates in the following manner:

- Dr. Bruno Gonçalves as a member of the staff of the Close Support Unit to the EFDA Associate Leader for JET;
- Dr. Duarte Borba as deputy Task Force Leader for TFM;
- Prof. Horácio Fernandes and Dr. Paulo Varela as members of the Remote Participation Users Group.